Overcoming the Tradeoff Between Processability and Mechanical Performance of Elastomeric Vitrimers

Georges Formon, Sonja Storch, Arnaud Y.-g. Delplanque, Bruno Bresson, Nathan van Zee, Renaud Nicolaÿ

Overcoming the Tradeoff between Processability and Mechanical Performance of Elastomeric Vitrimers

Georges J. M. Formon, Sonja Storch, Arnaud Y.-G. Delplanque, Bruno Bresson, Nathan J. Van Zee, and Renaud Nicolaÿ**

G. J. M. Formon, S. Storch, N. J. Van Zee, R. Nicolaÿ
Chimie Moléculaire, Macromoléculaire, Matériaux (C3M), UMR7617, ESPCI Paris, Université PSL, CNRS, 75005 Paris, France
E-mail: nathan.van-zee@espci.psl.eu; renaud.nicolay@espci.psl.eu

Bruno Bresson
Sciences et Ingénierie de la Matière Molle (SIMM), UMR 7615, ESPCI Paris, Université PSL, CNRS, 75005 Paris, France

Keywords: vitrimers, reactive extrusion, polymer blends, phase separation

Vitrimers are polymer networks with dynamic covalent bonds that allow the network to reconfigure its connectivity while maintaining a constant number of chemical bonds at all temperatures. The melt viscosity of vitrimers thus gradually decreases with temperature. This behavior makes vitrimers more difficult to process than typical thermoplastics using conventional processing techniques, such as extrusion. Although many strategies have been reported to address this issue, it remains challenging to overcome a key tradeoff between improving the processability or the mechanical performance. Herein, we present a new strategy for overcoming this tradeoff in the context of elastomeric vitrimers. Our approach entails the crosslinking of a functionalized low-T_g polymer matrix with an incompatible high-T_g polymer featuring pendant groups with complementary reactivity. When compared to a conventional homogeneous vitrimer, the microphase-separated materials prepared by reactive extrusion present improved tensile properties and creep resistance at room temperature while also exhibiting enhanced processability at high temperature. These enhanced properties are a consequence of the combination of the phase separation between the soft and hard phases, the restriction of dynamic crosslinking reactions within the interfacial zones, and the judicious selection of the T_g of the hard phase to be in between the use and processing temperatures.

1. INTRODUCTION

Over the past two decades, much research has been dedicated to exploiting dynamic covalent crosslinks as a means to create recyclable crosslinked materials, commonly known as covalent adaptable networks (CANs).[1–3] Vitrimers are a particular kind of CAN that features dynamic covalent crosslinks that undergo degenerate exchange reactions via an associative mechanism. This behavior causes the network to maintain a constant connectivity that is independent of temperature. The viscoelasticity of vitrimers is thus strongly impacted by the kinetics of the exchange reaction. Assuming an amorphous polymer matrix with a relatively low glass transition temperature (T_g), the material flows according to Arrhenius kinetics when it is heated above a characteristic network freezing temperature.[4,5] Originally developed on the basis of a metal-catalyzed transesterification reaction,[4] vitrimers and vitrimer-like materials have been exemplified using many different kinds of exchangeable functional groups, such as imines,[6] olefins,[7] carbonates,[8] hindered ureas,[9] vinylogous urethanes,[10] 1,2,3-triazoliums,[11] and boronic esters.[12] Vitrimers show promise for both the recycling[13,14] and upcycling[15,16] of polymer waste, especially for polyolefins,[17,18] epoxy resins,[4,19] polyurethanes[20–22] and polyesters.[23] Other notable applications include adhesion, additive manufacturing, shape memory, composite fabrication, and liquid crystalline elastomers.[24]

Our group has been particularly interested in the metathesis of boronic esters because it offers several advantages over other types of exchange chemistries. It is fast and does not require a catalyst, and boronic esters have excellent chemical orthogonality and thermo-oxidative stability.[25] However, in the context of elastomeric vitrimers, the ability of boronic esters to exchange even at room temperature can lead to poor creep resistance at service conditions.[26] Furthermore, boronic ester-based vitrimers can be more demanding to process compared to thermoplastic analogues owing to the Arrhenian temperature dependence of the melt viscosity.[5,25,27]

Although several examples of injectable and extrudable boronic ester-based vitrimers have been reported,[17,25,28,29] we have previously explored different strategies to further enhance the properties of such materials. For example, varying the crosslinking density modulates the viscosity and creep resistance of the material both at room and elevated temperatures, but it entails a tradeoff of a decreased T_g and inferior tensile properties.[25,26] Another approach is to incorporate a mixture of static and dynamic crosslinks. In the context of polybutadiene boronic ester-based vitrimers, we found that this strategy nearly doubles the creep resistance at room temperature while maintaining excellent mechanical recyclability. However, these double networks exhibit lower elongation and stress at break than their conventional vitrimer counterparts, and they are no longer suitable for extrusion or injection molding.[26] Other groups have employed static crosslinks in other kinds of vitrimers based on transesterification[30] and boronic ester metathesis,[31] and they also found that this strategy improves the dimensional stability of the material at the cost of processability.

Numerous other approaches have been reported to address this key tradeoff. For example, Guo[32] and Du[33] showed that the creep resistance at room temperature of styrene-butadiene rubber (SBR) boronic ester-based vitrimers is improved by incorporating metal-ligand coordination and hydrogen bonding, respectively. These secondary interactions act to create physical crosslinks and phase separation. Yu and co-workers[34] exemplified a multi-phase approach to preparing SBR boronic ester-based vitrimers by curing SBR in the presence of a dithiol bis(boronic ester) crosslinker and a ground powder of a highly-crosslinked SBR vitrimer. While the highly crosslinked vitrimer is not melt processable, the heterogeneous compositions are extrudable as cohesive strands. Sumerlin and colleagues showed that the relaxation dynamics of vinylogous urethane-based vitrimers can be modulated through microphase separation by using block-copolymers[35] and by changing the chain length of the thermoplastic precursors.[36] Du Prez and Winne[37] recently reported an approach for controlling the concentration of reactive groups as a function of temperature in step-growth vinylogous

urethane-based vitrimer, allowing for the suppression of creep at room temperature without decreasing processability at high temperatures.

All of these strategies, along with other advances such as latent catalysts and neighboring group effects,[38] can be used to tune vitrimer dynamics as a function of temperature to fulfill the need of reprocessable materials with high dimensional stability. However, these approaches generally achieve an improvement in only one aspect while being minimally detrimental to the other. It remains difficult to simultaneously enhance both the creep resistance at service temperatures and the processability of the network. In this context, we have developed a new strategy that combines microphase separation and functionalized polymers with complementary reactivity to address this challenge. As schematically depicted in **Figure 1**, in contrast to conventional crosslinking methods for making elastomeric vitrimers, we targeted a low-T_g matrix with functional groups that can react with an incompatible high-T_g polymer bearing functional groups with complementary reactivity. At relatively low temperature, this hard phase is designed to suppress exchange reactions and reinforce the low-T_g matrix. At high temperatures, the material is designed to flow more readily compared to conventional vitrimers owing to the crosslinking being limited to the interfacial zones. We anticipated that the properties of these materials would be highly dependent on the processing conditions, as they would dictate the size and morphology of the phase-separated domains.

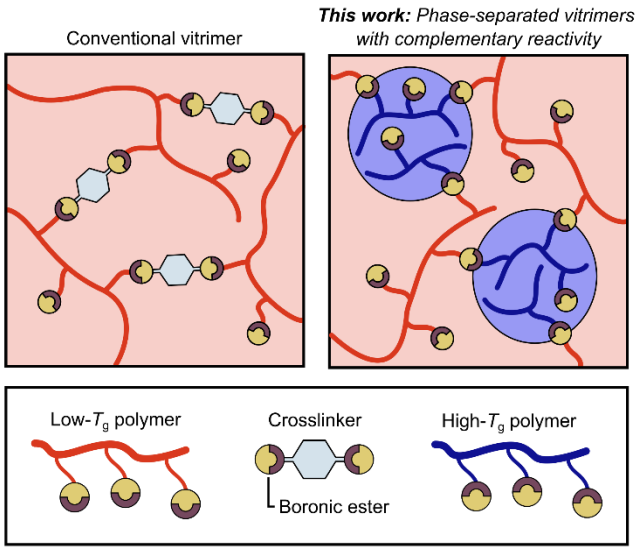

Figure 1. Schematic comparison between the structure of conventional vitrimer elastomers and the proposed phase-separated vitrimers featuring a high-T_g minor phase with reactivity complementary to that of the low-T_g major phase.

Herein, we exemplify this strategy using a series of polymethacrylate boronic ester-based vitrimers. We employed different processing conditions, including reactive processing and solvent blending, to create materials with distinct phase-separated morphologies. We then tested these compositions by dynamic mechanical analysis, rheological experiments, and tensile testing. As a point of reference for our new compositions, the same soft polymethacrylate precursor described above was crosslinked using a bis(boronic ester) unit to create a morphologically homogeneous elastomeric vitrimer.[25] The phase-separated materials obtained by reactive extrusion exhibit increased toughness or stiffness, depending on the synthetic protocol, with mechanical properties superior to those of the reference vitrimer. Furthermore, these materials feature an impressive combination of improved processability at high temperatures and enhanced creep resistance at room temperature.

2. RESULTS AND DISCUSSION

2.1. Design, synthesis, and characterization of the thermoplastic precursors

As depicted in Figure 1, we envisioned to create microphase-separated materials comprised of a reactive major soft phase and a dispersed hard polymer that possesses complementary reactivity. Two functionalized copolymers were thus targeted, one with a T_g below room temperature and the other with a T_g in between the use and processing temperatures. To achieve a phase separated morphology, the two copolymers need to be chemically distinct to be incompatible with each other.

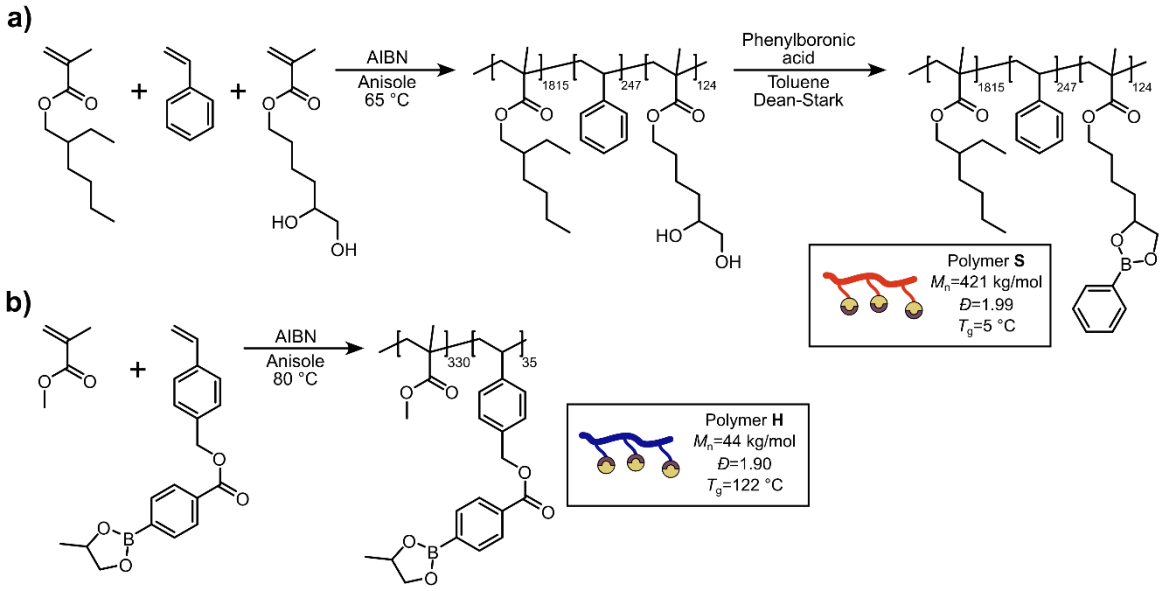

Figure 2. a) Synthesis of the low-T_g polymer **S** constituting the major soft phase. b) Synthesis of the high-T_g polymer **H** constituting the dispersed hard phase. c) Chemical structure of the crosslinker **BisBE**.

Based on ease of synthesis, we opted to focus on two functionalized polymethacrylates synthesized by free radical polymerization (FRP). The synthesis and chemical structures for the selected polymers are presented in **Figure 2**. The EHMA-based low-T_g polymer, designated as the soft phase **S**, features pendant boronic esters linked to the backbone through the diol moiety. The MMA-based high-T_g polymer, designated as the hard phase **H**, contains boronic ester side-groups linked to the backbone via the boron atom. Polymer **S,** with a T_g of 5 °C, has an M_n of 421 kg/mol (corresponding to a *DP* of 2190) and a dispersity of approximately 2 (Figure 2, S6A

and S7A and Table S1). An average functionality of 5.7 mol% was calculated based on monomer conversion evaluated by ^{1}H NMR spectroscopy, which translates to an average of 125 boronic esters per chain. Polymer **H**, with a T_g of 122 °C, was synthesized through FRP using a much larger amount of initiator as compared to the synthesis of **S**, resulting in M_n, *DP* and $Đ$ values of 44 kg/mol, 365 and 1.90, respectively (Figure 2, S6A and S7A and Table S1). The average functionalization degree is 9.5 mol%, giving an average of 35 boronic esters per chain. During radical copolymerizations of styrene-based monomers and methacrylates, the monomer used in default tend to copolymerize faster than the monomer used in excess. [39] Thus, a drift in composition was anticipated for both **S** and **H**. However, we judged that this structural feature will not dominate the properties of our materials (see the Supporting Information for further discussion).

To achieve desirable elastomeric properties for the phase-separated materials, we targeted a 10 wt% loading of the high-T_g phase **H** to be dispersed in the low-T_g **S** phase, which would give a ratio of pendant boronic esters between the **S** and **H** phases of 3.4. If we assume isoreactivity (i.e., $K_{eq} = 1$) of all the dioxaborolanes present in the systems, and consider that the equilibrium constant of the exchange reaction between the two functional polymers is equal to unity, this stoichiometric ratio would result in a conversion of 23% of the boronic esters of **S** (77% of **H**). With these considerations in mind, **S** should theoretically contain a maximum of 28.3 crosslinks per chain on average (i.e., one crosslink every 77 monomer units).

Compatibility was another important factor in designing the structure of **S** and **H**. Block copolymers of EHMA and MMA have been reported to exhibit nanophase separation,[40] suggesting that the corresponding homopolymers are incompatible. Nevertheless, given the similarity of their chemical structures, we hypothesized that the interface between these two polymers would be relatively broad, which is favorable for interfacial reactions to occur during reactive processing.[41]

Polymers **S** and **H** were characterized by DMA and small-amplitude oscillatory shear (SAOS) rheology (Figure S9, S10 and S11). As anticipated, **S** exhibits an elastic storage modulus (*G*') above the T_g due to entanglements up to 150 °C (Figure S9a). The glass transition is broad and approximately 30 °C above what is observed by DSC (Table S1 and S2). Multi-temperature SAOS experiments and successful application of time-temperature superposition confirm this behavior with a rubbery region spanning over four decades in frequency (Figure S10). This material is a soft and malleable solid at room temperature that can be easily compression molded at a temperature as low as 100 °C. Polymer **H** shows signs of being close to the gel point by both DMA and SAOS experiments (Figure S9b and S11). The rubbery region covers a larger range of frequencies than what is expected based on the number of entanglements at this molecular weight (i.e., 6 entanglements per chain),[39] which is most likely due to the formation of trace amounts of boroxines during isolation and processing. Although no boroxine groups are detected by ^{1}H NMR spectroscopy (Figure S4), a trace conversion of the pendant boronic esters, even less than 1%, could be responsible for this effect. Nevertheless, **H** is still a viscoelastic liquid at high temperatures, as the crossover of the loss (G") and storage (G') moduli are observed above 160 °C (Figure S11).

Flow curves were also performed for the two thermoplastic precursors at 180, 200, and 220 °C over a shear rate range of 10^{-4} to 10^{-1} s^{-1} (Figure S12). Both polymers show shear thinning behavior, although **S** nearly reaches a Newtonian plateau under these conditions. Between 180 and 220 °C, **H** is more viscous than **S**, however at 220 °C their viscosities approach each other, with their ratio (η_H/η_S) reaching unity at a shear rate of 0.1 s^{-1}. Polymers **S** and **H** were found to be stable well-above these temperatures based on TGA (Figure S8). These measurements were used to rationally design the extrusion protocol as described below.

2.2. Processing conditions for modulating the phase separation.

To have a homogeneous vitrimer as a point of reference throughout this study, polymer **S** was crosslinked using the bis(boronic ester) **BisBE** (Figure 2c) via solvent mixing and subsequent removal of the solvent (**Figure 3a**). This approach has been widely used in the community for making boronic ester-based vitrimers.[5] Our team has specifically used it to make other kinds of polymethacrylate vitrimers.[25]

In general, the morphology of phase-separated polymers is highly influenced by processing conditions. Our strategy for modulating the reactive dispersion of **H** within **S** is schematically depicted in Figure 3b and 3c. As indicated above, all compositions have a fixed **S**:**H** weight ratio of 9:1. One method is based on solvent mixing (Figure 3b) and two methods are based on reactive extrusion (Figure 3c), which are particularly appealing because reactive extrusion is fast, solvent-free, and industrially relevant. Even though all of these compositions contained the same weight ratio of **S** and **H**, the different processing conditions were expected to strongly influence the size and dispersion of the hard **H** phase within the soft **S** matrix.

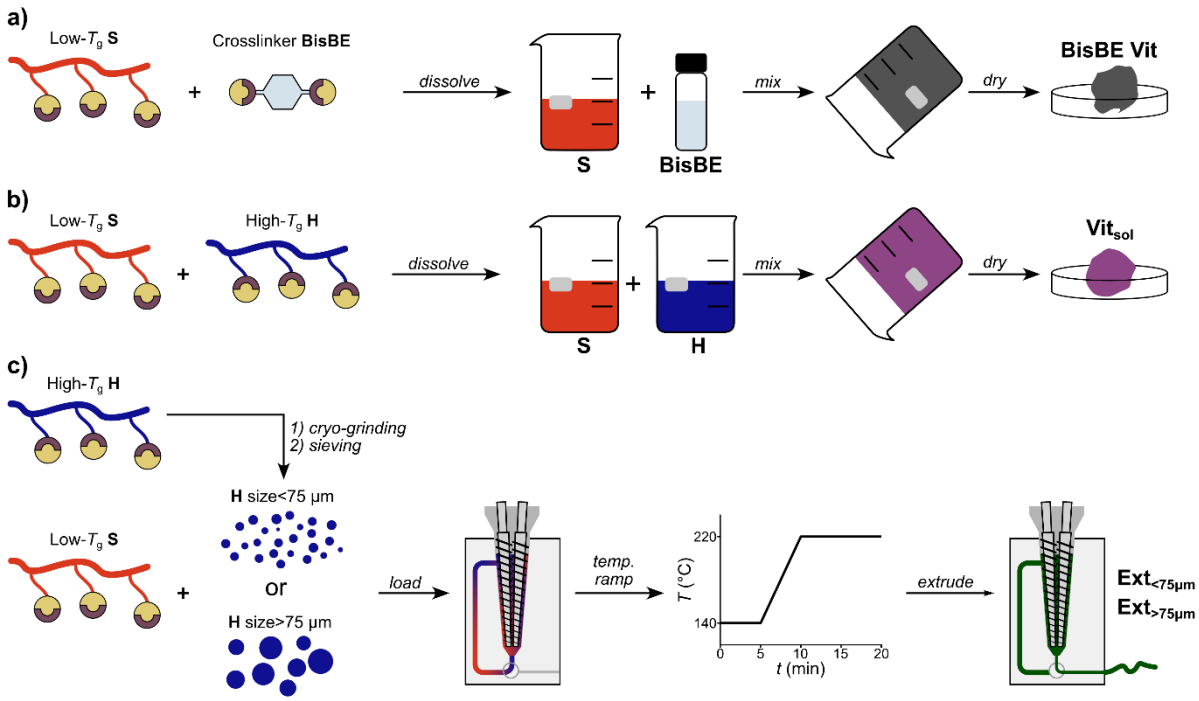

Figure 3. Schematic representation of the different vitrimer synthesis methods. a) Conventional crosslinking of **S** with the bis(boronic ester) crosslinker **BisBE** to give **BisBE Vit**. b) Solution-based mixing of **H** with **S** to give $\mathbf{Vit_{sol}}$. c) Reactive extrusion of **H** (after cryo-grinding and sieving) with **S** to yield $\mathbf{Ext_{<75µm}}$ and $\mathbf{Ext_{>75µm}}$.

The vitrimer formed using **S** and **BisBE** (Figure 3a) was synthesized using a modified report from the literature.[25] Polymer **S** was dissolved in dichloromethane (DCM), after which the crosslinker **BisBE** was added. To make the resulting vitrimer comparable to the polymer-polymer vitrimers, a molar ratio of 3.4 was chosen between the pendant boronic esters of S and the boronic esters of **BisBE**. Gelation was observed after approximately 1 h. The resulting gel was dried to yield **BisBE Vit**. To prepare the blend of **S** and **H** by solvent mixing (Figure 3b), each polymer was dissolved in DCM, and then the two solutions were mixed to reach the targeted 9:1 **S** to **H** weight ratio. Gelation was observed in less than 5 min. The solvent was removed from the gel to yield **Vit$_{sol}$**. Comparable polymer-polymer vitrimers prepared in an analogous way have already been reported,[42] but the present system is distinguished by being an incompatible hard-soft thermoplastic pair.

To prepare blends by reactive extrusion (Figure 3c), polymer **H** was first cryogenically ground and then passed through a 75 µm sieve to separate the material into two particle size ranges, one above and one below 75 µm. Polymer **S** was then loaded with one of these ground **H** samples into an extruder at 140 °C and 50 rpm screw speed. Once loading was complete, the speed of the screws was increased to 200 rpm, and these conditions were maintained for 5 min. This pre-mixing stage was inspired by our previous work on polyethylene vitrimers[17] and was implemented to improve mixing and reproducibility. The temperature was then increased to 220 °C for 10 min, which is the temperature at which the viscosities of **H** and **S** are the closest to each other (Figure S12) and expected to improve the dispersion of the incompatible phase by reducing the droplet size.[43] The screw speed of 200 rpm was chosen because high shear rates has also been found to increase the interfacial surface area between incompatible polymers in reactive extrusion, thereby increasing the rate of reaction.[44]

This protocol was used to prepare two materials with different size ranges of the ground **H** hard phase: **Ext$_{<75µm}$**, which was made using particles of **H** with particle size less than 75 µm, and **Ext$_{>75µm}$**, which was made with **H** powder that did not pass through the 75 µm sieve. The

extrusion profiles (Figure S13) reveal that a plateau in the torque is rapidly achieved, indicating that the system reaches a steady state. The TGA profiles for these and the other vitrimers prepared via solvent-mixing demonstrate that all networks exhibit similar thermal stability to the polymer precursors **S** and **H** (Figure S8).

2.3. Morphological analysis of polymer-polymer vitrimers.

We sought to distinguish the morphologies of these different vitrimers to establish a basis for rationalizing their thermomechanical and processing properties. First, **BisBE Vit** did not present phase separation or the formation of aggregates on the basis of scanning electron microscopy (SEM, Figure S14). Moreover, discs made from this vitrimer exhibited high optical clarity (Figure S15). In contrast, **Vit$_{sol}$** exhibits a rich nanostructure. Based on small angle X-ray scattering experiments at room temperature, it exhibits a broad peak at a scattering vector q centered at approximately 0.3 nm^{-1}, corresponding to a distance of 20 nm (**Figure 4a**). In the low q region ($0.02 < q < 0.1$ nm^{-1}), the scaling of this curve in a log-log plot is −2.9 (Figure S16), which suggests scattering from a mass fractal.[45] The lack of sharp Bragg peaks further indicates that the aggregates are not densely packed.

Taking inspiration from a recent study on the nanostructure of polyethylene vitrimers in the melt,[46] we hypothesized that the SAXS pattern of **Vit$_{sol}$** could be fit to an aggregate-fractal scattering model (Figure S17 and Table S3). Following a log-normal distribution, we calculated that the spheres have an average diameter of 5.6 nm with a dispersity of 0.3 (i.e., standard deviation divided by the mean). The fractal dimension was calculated to be 3, consistent with the slope measured in the low-q region in Figure S16, and it corresponds to a continuous, isotropic, three-dimensional constellation of assembled spheres.[47]

Imaging by atomic force microscopy (AFM) corroborates this morphological proposal for **Vit$_{sol}$**. Phase profiles of the surface show spheres of approximately 10 nm that aggregate into larger assemblies, forming clusters and networks of spheres (Figure 4b and S18). The contrast in phase is derived from differences in the mechanical properties between the matrix and the

particles, which we interpret as corresponding to the differences between **S**-rich and **H**-rich regions, respectively, based on the difference in T_g between these two polymers. The areas with high phase angle are most likely **H**-rich, due to higher stiffness, while the lower phase angle region is most likely **S**-rich.[48] These AFM results are in excellent agreement with the SAXS results and support our choice of model.

The fractured surface of **Vit$_{sol}$** was also observed by SEM (Figure S19), showing a textured surface with nanoscopic protuberances, similar to the observations made by AFM. However, the aggregates appear larger in these images because the sample was coated with a 5 nm gold layer, which is on the same order of magnitude as the size of the aggregates.

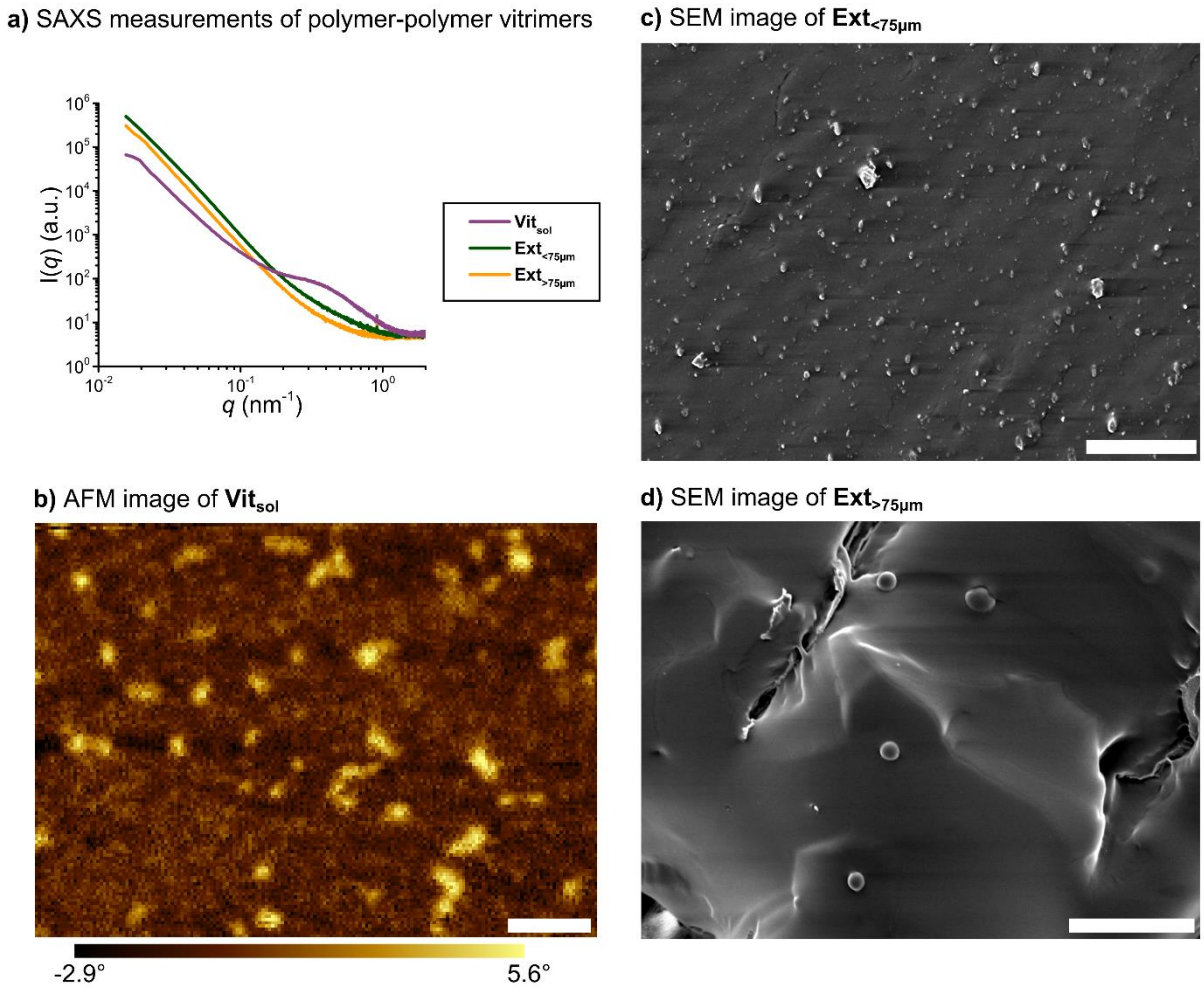

Figure 4. a) SAXS, scattered intensity as a function of scattering vector, of **Ext$_{<75µm}$**, **Ext$_{>75µm}$** and **Vit$_{sol}$**. b) AFM phase mapping of **Vit$_{sol}$**. Scale bar is 100 nm. c) and d) Representative SEM pictures of **Ext$_{<75µm}$** and **Ext$_{>75µm}$**, respectively, soft fractured surfaces. Scale bars are 20 µm.

As for the samples prepared by reactive extrusion, **Ext**$_{<75\mu m}$ and **Ext**$_{>75\mu m}$ do not present any prominent features based on SAXS measurements, suggesting that the particles of **H** in **S** are larger than what can be detected by SAXS (Figure 4a). In the low-q region, the scattering intensity scales as $I \sim q^{-3.5}$ for both samples (Figure S16b and c); this positive deviation from Porod's law (i.e., exponent of −3.5 instead of the predicted −4) is an indication that the surface of the particles is either fractally rough and/or that the particles are highly polydisperse. In our case, both conditions are likely true.[49]

The extruded vitrimers **Ext**$_{<75\mu m}$ and **Ext**$_{>75\mu m}$ were thus further studied by SEM (Figure 4c and d, S20 and S21). The samples were fractured either at room temperature or at 70 °C (i.e., above the glass transition of **S** but below that of **H**). This technique allows for **H** particles to remain intact and observable by SEM.[50] The most striking feature in these micrographs is that the particles are polydisperse in size, ranging from hundreds of nanometers to a few microns. Particle analysis (See the Supporting Information for a description of the process, Figure S22, and Table S4) yields an average particle size of 0.48 µm for **Ext**$_{<75\mu m}$, and 4.0 µm for **Ext**$_{>75\mu m}$, with dispersities (i.e., standard deviation divided by the mean) of 0.77 and 0.95, respectively. Consistent with the discrepancy of particle size introduced during sample preparation, the average size of the aggregates in **Ext**$_{>75\mu m}$ are almost an order of magnitude larger than in **Ext**$_{<75\mu m}$. Furthermore, the shape of the **H** domains in **Ext**$_{>75\mu m}$ seem more spherical and homogeneous than in **Ext**$_{<75\mu m}$, which have a less defined structure.

To further understand the impact of the morphology on network formation, we evaluated the gel fraction of each sample after swelling in chloroform at room temperature for 24 h. **BisBE Vit** is almost completely soluble with only 6±8% insoluble portion. This result is due to the fast dynamics of boronic ester metathesis, leading to a rapid change in topology in solvent to form loops and branches that cause the material to dissolve without decreasing the overall number of chemical bonds. These processes are facilitated by the large amount of free boronic ester (around 90 per chain) and the use of a difunctional crosslinker.[5,26]

The polymer-polymer vitrimers display strikingly different behavior, with **Vit$_{sol}$**, **Ext$_{<75\mu m}$**, and **Ext$_{>75\mu m}$** exhibiting gel fractions of 92±1%, 81±3% and 51±6%, respectively. Given the multivalent nature of the crosslinking via the reaction of complementary polymers, it is expected that these materials will have a reduced tendency to form soluble branched and looped structures. A competing factor is that the crosslinking reactions will only occur within the interfacial zone; thus, the gel fraction is expected to depend on the dispersion of the phases. The trend of gel fractions across these samples reflects both factors. First, all of these samples exhibit a higher gel fraction than **BisBE Vit**. Secondly, the trend in gel fraction going from **Vit$_{sol}$** to **Ext$_{<75\mu m}$** to **Ext$_{>75\mu m}$** is negatively correlated with the average size of the **H** domains in each sample and, given that the same loading of **H** was used in each sample, positively correlated with the total surface area of the **H** domains. The high gel fraction that we obtain for the extruded materials reinforce the notion that these materials are vitrimers.[5,17,25,26,46]

2.4. Phase-separation allows for tuning the thermomechanical profile.

The morphological study presented above establishes that the different protocols used for reactively blending **S** and **H** have a striking impact on the dispersion of the incompatible hard phase within the soft matrix, with average particle sizes ranging from approximately 10 nm to 4 μm. Since these polymers have complementary reactivity, morphological differences directly dictate the degree of network formation. Below, using **BisBE Vit** as the representative benchmark for a homogeneous vitrimer, we focus on elucidating the impact of these structural differences on the mechanical properties and, in the subsequent section, the processability of these materials.

In preparation for thermomechanical testing, each material was compression molded at 220 °C, for 10 min in the case of **BisBE Vit** and **Vit$_{sol}$** and for 5 min in the case of **Ext$_{<75\mu m}$** and **Ext$_{>75\mu m}$.** Based on DMA (**Figure 5**), **BisBE Vit** behaves like a typical vitrimer with a rubbery plateau at temperatures above the T_g with a value of approximately 0.4 MPa (Figure 5 and S23a).

Vit$_{sol}$ exhibits two glass transitions, corresponding to the phase-separated **S** and **H** domains. The first transition is readily apparent by DSC (Figure S7b), while the second is more prominent by DMA (Figure 5 and S23b). A rubbery plateau is observed at temperatures above the T_g of the **H** phase at 0.5 MPa, which is nearly identical to that observed for **BisBE Vit**. The superimposition of the modulus of the plateau was expected because the materials have the same targeted crosslinking density (see above). Additionally, the intimate mixing of the **H** and **S** phases in **Vit$_{sol}$** allowed it to essentially behave like the homogeneous vitrimer at temperatures above the T_g of the **H** phase.

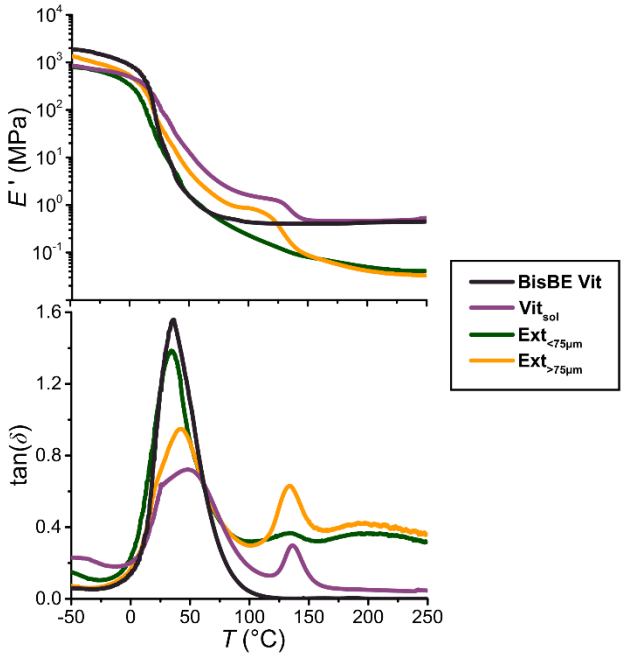

Figure 5. Extensional storage modulus *E*' (top) and loss factor tan(δ) (bottom) as a function of temperature from DMA of **BisBE Vit**, **Vit$_{sol}$**, **Ext$_{<75µm}$**, and **Ext$_{>75µm}$**.

The extruded materials behave distinctly differently compared to **BisBE Vit** and **Vit$_{sol}$**. In the case of **Ext$_{<75µm}$** (Figure 5 and S23c), a sharp T_g attributed to the **S** phase is observed, but the T_g of the **H** phase at 134 °C is detected as a weak transition in the tan(δ) curve. The same effect is observed by DSC (Figure S7b), with the T_g of the **S** phase being more prominent than the one of the **H** phase. **Ext$_{<75µm}$** does not exhibit a rubbery plateau, but rather an elastic storage modulus (*E*') that gradually decreases from 70 kPa at 160 °C to 40 kPa at 250 °C. As for **Ext$_{>75µm}$**, it clearly presents the two glass transitions for the **S** and **H** phases based on both DMA

and DSC (Figure 5, S7b and S23d). Above the second T_g, E' gradually decreases in a very similar way as described above for **Ext$_{<75\mu m}$**.

It was surprising that the T_g of the **H** phase in **Ext$_{<75\mu m}$** was less prominent than in **Vit$_{sol}$** despite featuring a coarser morphology. We suspect that this discrepancy is due to a difference in sample preparation. **Vit$_{sol}$** was dried over 24 hours at room temperature and then overnight at 150 °C to completely remove the solvent used for synthesis; this protocol also served as a long annealing process. The solvent likely acted as plasticizer, facilitating the complete relaxation of this material. In contrast, for preparing **Ext$_{<75\mu m}$**, **H** was cryo-ground and then reacted with **S** by solvent-free reactive extrusion, resulting in a material that is far less relaxed compared to **Vit$_{sol}$**. In the case of **Ext$_{>75\mu m}$**, the **H** particles are much larger than in **Ext$_{<75\mu m}$**, allowing the core of the particles to be isolated from the interface, thereby resembling bulk **H** despite also being subjected to reactive extrusion.

The mechanical performance of this family of materials was probed by uniaxial tensile testing. Measurements were performed at room temperature. Given that the measurements were performed at 100%/min, corresponding to a frequency of approximately 0.1 rad/s, the materials are all in a similar range close to the rubbery region based on the frequency sweep measurements at 30 °C (Figure 7, blue curves; see below). Representative engineering stress-strain curves and the calculated tensile properties are plotted in **Figure 6** (the full set of curves is presented in Figure S24). As the point of reference, **BisBE Vit** is a ductile material with a strain at break of 310±30% and a Young's modulus of 2.2±0.2 MPa. **Vit$_{sol}$** is much stiffer than **BisBE Vit**, with both a higher Young's modulus and stress at break. It is less ductile than **BisBE Vit** with an elongation at break of 240±14%.

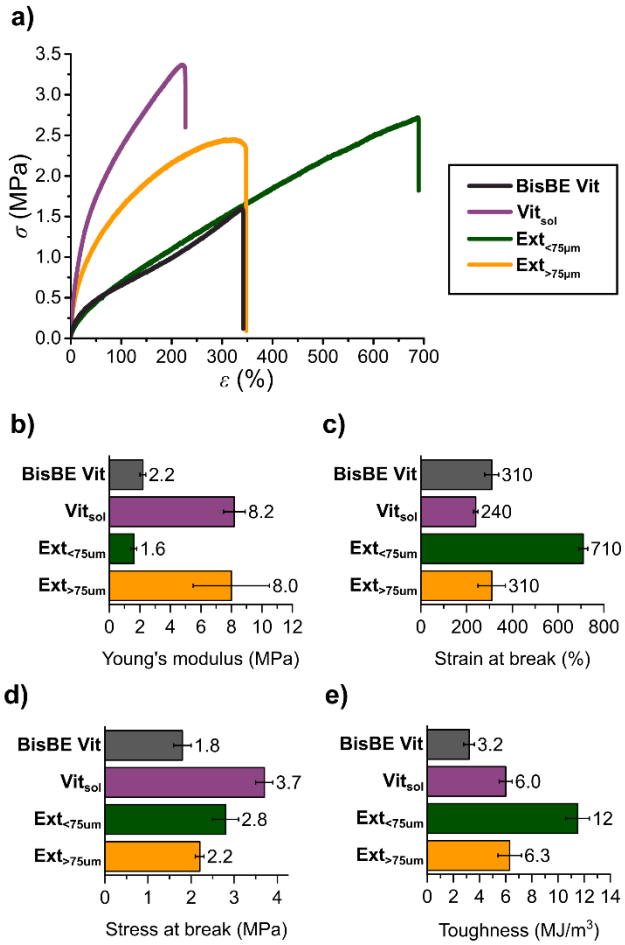

Figure 6. a) Representative curves of uniaxial tensile test, engineering stress *versus* strain, of **BisBE Vit**, **Vit$_{sol}$**, **Ext$_{<75\mu m}$**, and **Ext$_{>75\mu m}$**. Calculated: b) Young's Modulus; c) Strain at break; d) Stress at break; e) Toughness of **BisBE Vit**, **Vit$_{sol}$**, **Ext$_{<75\mu m}$**, and **Ext$_{>75\mu m}$**. Values displayed are the average of quintuplicate measurements, while the error bars are the standard deviation.

The extruded materials exhibit remarkable improvements in tensile properties compared to **BisBE Vit** (Figure 6). **Ext$_{<75\mu m}$** is the most ductile material in this study, breaking at a strain of 710±20%. Strikingly, the low-strain region of the stress-strain curve is very similar to that of **BisBE Vit**, but it breaks at more than double the strain and 55% higher stress, albeit with a slightly smaller Young's modulus. **Ext$_{>75\mu m}$** is much stiffer than **BisBE Vit**, having a larger Young's modulus of 8.0±2.5 MPa and a comparable stress at break of 2.2±0.1 MPa, while maintaining essentially the same degree of ductility. In terms of toughness, all of the polymer-polymer materials are tougher than **BisBE Vit**, with **Ext$_{<75\mu m}$** exhibiting superior performance based on this metric.

These results demonstrate that the combination of complementary reactivity between incompatible phases and morphological control can be exploited to improve tensile properties at room temperature compared to a conventional homogeneous vitrimer**.** The high-T_g **H** phase strongly reinforces the elastomeric low-T_g **S** matrix, and the size of these domains dictates whether the material exhibits enhanced stiffness or ductility. Most compellingly, the extruded materials **Ext**$_{<75\mu m}$ and **Ext**$_{>75\mu m}$ exhibit comprehensively superior tensile properties over **BisBE Vit**.

2.5. Phase-separation enhances creep resistance at low temperature and fluidity at high temperature.

Finally, processability was assessed based on a series of rheological measurements. Multi-temperature SAOS experiments were performed at 160, 120, 80, and 30 °C (**Figure 7**). **BisBE Vit** displays a plateau with a constant shear storage modulus (*G*') of approximately 0.11 MPa (ω=1 rad/s) between 80 and 160 °C. As the temperature is increased, the shear loss modulus (*G*") becomes close to *G*' in the lower angular frequency region, hinting at the beginning of the viscous terminal regime. In comparison, **Vit**$_{sol}$ also displays a plateau between 80 and 160 °C, but *G*' decreases by almost a factor of 2, going from 0.26 MPa at 80 to 0.15 MPa °C at 160 °C (ω=1 rad/s). This behavior is most likely due to the glass transition of **H** (T_g = 122 °C) and is consistent with DMA (Figure 5).

For **Ext**$_{<75\mu m}$ and **Ext**$_{>75\mu m}$, the viscoelastic spectra are strikingly different. For both extruded materials, no plateau is observed, and *G*' undergoes a sharp drop as the temperature is increased from 80 to 160 °C; at a radial frequency of 1 rad/s, *G*' decreases by a factor of 11 for **Ext**$_{<75\mu m}$ and by a factor of 23 for **Ext**$_{>75\mu m}$. At the highest temperatures, we observe the crossover of *G*' and *G*" at angular frequencies of 0.3 rad/s for **Ext**$_{<75\mu m}$ and 0.2 rad/s for **Ext**$_{>75\mu m}$, corresponding to terminal relaxation times of 3.3 and 5.0 s, respectively.

We interpret these features as being a consequence of both the phase-separated nature of these samples and the complementary reactivity of the two phases. Since not all of the soft phase **S** can simultaneously participate in dynamic crosslinking reactions at the interface with the hard phase **H**, there is a fluxional population of polymer chains that are not part of the chemical network. These chains likely serve as a kind of reactive lubricant for the system, resulting in a material that is easier to process (as reflected in the extrusion profile with low torque in Figure S13). Additionally, the processing temperature is well above the T_g of the hard phase, which allows exchange reactions to more easily occur within the interfacial region, thereby improving the material's ability to flow.

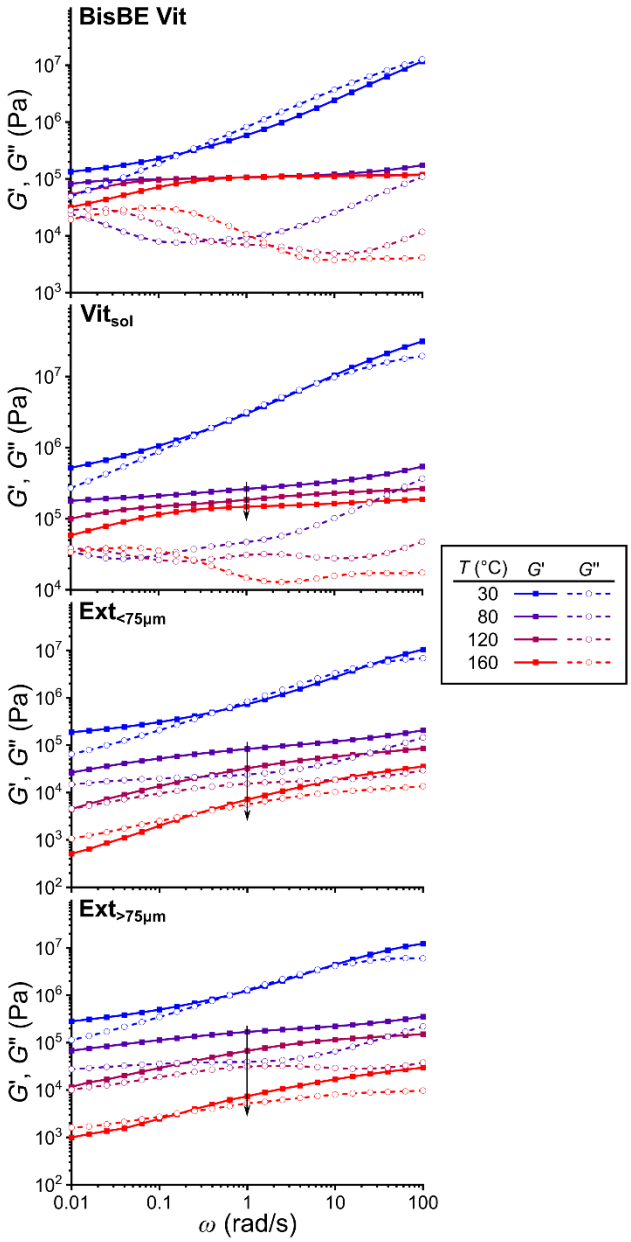

Figure 7. Comparison of the multi-temperature frequency sweeps for **BisBE Vit**, **Vit$_{sol}$**, **Ext$_{<75µm}$**, and **Ext$_{>75µm}$**. Shear storage (*G*') and loss (*G*") moduli are plotted as a function of frequency. The black arrows highlight the decrease of *G*' going from 80 to 160 °C for samples **Vit$_{sol}$**, **Ext$_{<75µm}$**, and **Ext$_{>75µm}$**.

To further probe the processability of these materials, creep-recovery experiments were conducted at 160 °C. We take inspiration from recent work in which creep experiments were particularly useful for benchmarking the flow properties of phase-separated polyolefin vitrimers.[51] The first creep and recovery cycle for all samples at 160 °C is presented in **Figure 8a**. After 30 min with a constant stress of 50 Pa, **BisBE Vit** and **Vit$_{sol}$** creep 1.3 and 0.17%, respectively, and the residual strain is 0.38 and 0.01%, respectively, after 30 min of recovery.

In stark contrast, **Ext**$_{<75\mu m}$ and **Ext**$_{<75\mu m}$ creep 39 and 23% after 30 minutes under the same conditions. After half an hour recovery, these materials return to 33 and 19 % strain, respectively, which is consistent with the increased ability to flow that was observed in the frequency sweep experiments.

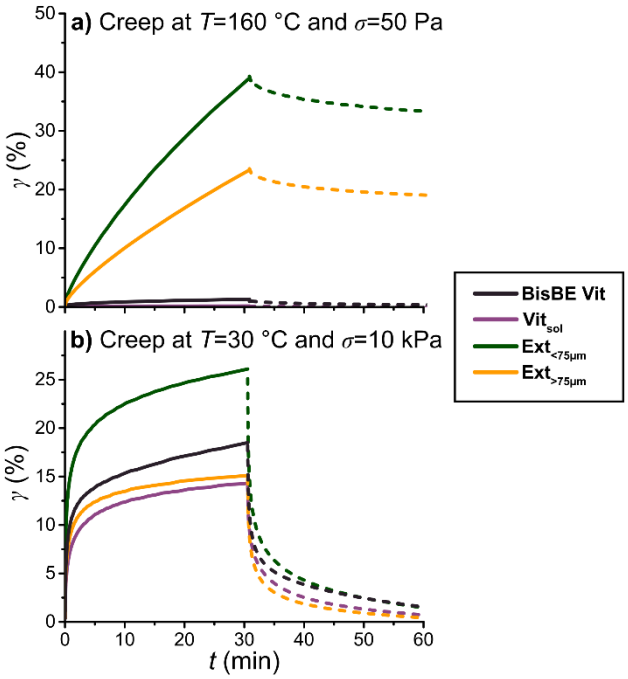

Figure 8. Creep and recovery curves, shear strain as a function of time, of **BisBE Vit**, **Vit**$_{sol}$, **Ext**$_{<75\mu m}$, and **Ext**$_{>75\mu m}$ at a) 160 °C with an applied stress σ of 50 Pa and b) 30 °C with an applied stress σ of 10 kPa. Creep and recovery are represented by solid and dashed lines respectively.

We performed successive creep-recovery cycles at 160 °C to assess the evolution of viscoelastic properties with time. Although **BisBE Vit** and **Vit**$_{sol}$ displayed stable creep-recovery performance over four sequential creep-recovery cycles, the curves for the extruded samples did not superimpose, with creep decreasing after each cycle (Figure S25). To gain insight into this behavior, SEM was performed on the fractured surfaces of samples of **Ext**$_{<75\mu m}$ and **Ext**$_{>75\mu m}$ that had undergone four sequential creep-recovery experiments (Figure S26 and

S27 and Table S5). In comparison with the structure of the as-prepared materials (Figure 4c and d, S20, and S21), the average size of the particles increased by 17 and 70 % in **Ext$_{<75\mu m}$** and **Ext$_{>75\mu m}$**, respectively; however, these values are within the standard deviations reported for each sample before the creep experiments (Table S4). In the case of **Ext$_{>75\mu m}$**, the surface of the particles featured a notably rougher texture after the creep experiments (Figure S27d). This behavior results in an increase in the surface area of the particles, which could allow for more interfacial crosslinking reactions to take place, thereby impacting the relaxation dynamics of these materials.

We compared the creep compliance, $J(t)$, after the first and fourth cycles to further illuminate how the viscoelasticity of these materials evolves at high temperature (Figure S28). The power law scaling of $J(t)$ is expected to be unity when a material reaches terminal relaxation.[52] Ricarte et al.[51] recently demonstrated that the $J(t)$ scaling behavior is a useful, model-free approach for comparing the ability of vitrimers to flow. For **Ext$_{<75\mu m}$** and **Ext$_{>75\mu m}$**, although $J(t)$ deviates at short timescale in going from the first to fourth cycle, all curves reach similar power law scaling after 30 min. For instance, the scaling of $J(t)$ for **Ext$_{<75\mu m}$** reaches 0.70 to 0.75 at the end of the creep step on the first and fourth cycles, respectively, while $J(t)$ for **Ext$_{>75\mu m}$** reaches scaling values of 0.77 and 0.74 on the first and fourth cycles, respectively. Thus, these samples appear to undergo a subtle structural evolution over time at high temperature that affects the relaxation dynamics at short times scales within the linear regime, but ultimately they reach similar flow kinetics at longer time. Moreover, these extruded samples attain scaling behavior that is closer to terminal relaxation than **BisBE Vit** and **Vit$_{sol}$**, as they reach scaling of 0.33 and 0.21 after 30 minutes on the fourth cycle, respectively (Figure S28b). We believe that the faster relaxation dynamics observed for **Ext$_{<75\mu m}$** and **Ext$_{>75\mu m}$** with these high-temperature creep experiments are further evidience for the enhanced processibility afforded by their explicitly heterogeneous structures.

Finally, to assess the dimensional stability of these samples at use temperature, creep-recovery experiments were performed at 30 °C for 30 minutes with an applied stress of 10 kPa, followed by 30 minutes of recovery (Figure 8b). **BisBE Vit** reached a strain of 19% after 30 min, and after recovery the residual deformation was 1.4%. By comparison, **Vit$_{sol}$** reached a deformation of 14% and was left with 0.66% deformation after recovery. As for the extruded materials, **Ext$_{<75\mu m}$** exhibited the largest initial deformation at 26%, but after recovery it matched the performance of **BisBE Vit** with only 1.4% residual strain. Finally, **Ext$_{>75\mu m}$** reached an initial deformation of 15%, and after recover only 0.39% strain remained. This result represents an improvement in creep resistance by a factor of 3.7 over the **BisBE Vit** reference material.

We propose that the striking performance of the extruded materials in creep experiments at room temperature is primarily attributable to their phase-separated nature and the judicious choice of the T_g of the hard phase. During processing, transiently free chains that are not incorporated in the network structure act to lubricate the system during processing; the hard phase is also softened because the material is processed at temperatures well above its T_g. At use temperature, the dynamicity of the network within the interfacial zones is strongly retarded by the glassy the hard phase, which serves to further reinforce the matrix. Moreover, these glassy modules act as a reinforcing agent, akin to the design of thermoplastic vulcanizates.[53]

3. CONCLUSION

We have developed a new strategy for simultaneously improving the dimensional stability and the processability of elastomeric vitrimers. The approach entails the use of an incompatible high-T_g polymer as a crosslinker for a low-T_g polymer matrix functionalized with groups with complementary reactivity. These networks were prepared by both solvent blending and reactive extrusion, for which the particle size of the minor high-T_g phase can be controlled by sieving. A morphological study by SAXS, AFM, and SEM of the resulting materials revealed that the

different processing conditions strongly influenced the size and distribution of the incompatible hard phase, ranging from the nanoscale for the solvent blended system to the microscale for the extruded materials. Gel fraction experiments revealed a negative correlation between the particle size and the degree of network formation.

We then performed a series of thermomechanical and rheological experiments to benchmark the performance of these phase-separated materials against that of a morphologically homogeneous vitrimer that was prepared by conventional methods. Remarkably, we found that the extruded phase-separated materials exhibit comprehensively improved tensile properties; the material can be tuned toward being stiffer or more ductile depending on its morphology. Even more striking, these same materials exhibit both enhanced fluidity at high temperature based on SAOS and creep-recovery experiments, and enhanced creep resistance at low temperature. We propose that these impressive properties are a consequence of the combination of phase separation, crosslinking reactions only occurring within the interfacial zones, and judicious selection of the T_g of the hard phase to be in between use and processing temperatures. The fact that these materials were obtained by reactive extrusion is particularly appealing because of its industrial relevance.

Further investigation is still needed to better comprehend the structure-property relationships for these materials. Parameters that are of interest for future study are feeding of monodisperse particles, reaction conditions, annealing and the addition of compatibilizers. We anticipate that this strategy could be general use to improving the properties of not only vitrimers but CANs in general. This work paves the way for new modular materials that can be rapidly accessed and tailored for a specific need based on simple design principles.

Supporting Information

Supporting Information which includes the experimental section and supplemental figures is available as a PDF file free of charge.

Acknowledgements

The Institute Carnot IPGG Microfluidique is gratefully acknowledged for partially funding this work (Appel à Projet C.A.R.N.O.T.). Mickaël Pomes-Hadda is gratefully acknowledged for his help in performing thermogravimetric analysis and rheological measurements. We acknowledge SOLEIL for provision of synchrotron radiation facilities (proposal No. 20220576) and we would like to thank Thomas Bizien for assistance in using the beamline SWING. We would like to thank Clement Guibert and Thomas Vialon for help on the collection and interpretation of the SAXS data. This work benefited from the use of the SasView application, originally developed under NSF award DMR-0520547. SasView contains code developed with funding from the European Union's Horizon 2020 research and innovation programme under the SINE2020 project, grant agreement No. 654000.

References

[1] J.-M. Lehn, *Prog. Polym. Sci.* **2005**, *30*, 814.
[2] X. Yan, F. Wang, B. Zheng, F. Huang, *Chem. Soc. Rev.* **2012**, *41*, 6042.
[3] C. J. Kloxin, C. N. Bowman, *Chem Soc Rev* **2013**, *42*, 7161.
[4] D. Montarnal, M. Capelot, F. Tournilhac, L. Leibler, *Science* **2011**, *334*, 965.
[5] N. J. Van Zee, R. Nicolaÿ, *Prog. Polym. Sci.* **2020**, *104*, 101233.
[6] P. Taynton, K. Yu, R. K. Shoemaker, Y. Jin, H. J. Qi, W. Zhang, *Adv. Mater.* **2014**, *26*, 3938.
[7] Y.-X. Lu, F. Tournilhac, L. Leibler, Z. Guan, *J. Am. Chem. Soc.* **2012**, *134*, 8424.
[8] R. L. Snyder, D. J. Fortman, G. X. De Hoe, M. A. Hillmyer, W. R. Dichtel, *Macromolecules* **2018**, *51*, 389.
[9] H. Ying, Y. Zhang, J. Cheng, *Nat. Commun.* **2014**, *5*, 3218.
[10] W. Denissen, G. Rivero, R. Nicolaÿ, L. Leibler, J. M. Winne, F. E. Du Prez, *Adv. Funct. Mater.* **2015**, *25*, 2451.
[11] M. M. Obadia, A. Jourdain, P. Cassagnau, D. Montarnal, E. Drockenmuller, *Adv. Funct. Mater.* **2017**, *27*, 1703258.
[12] M. Gosecki, M. Gosecka, *Polymers* **2022**, *14*, 842.
[13] D. J. Fortman, J. P. Brutman, G. X. De Hoe, R. L. Snyder, W. R. Dichtel, M. A. Hillmyer, *ACS Sustain. Chem. Eng.* **2018**, *6*, 11145.
[14] T. H. Epps, L. T. J. Korley, T. Yan, K. L. Beers, T. M. Burt, *JACS Au* **2022**, *2*, 3.
[15] C. Jehanno, J. W. Alty, M. Roosen, S. De Meester, A. P. Dove, E. Y.-X. Chen, F. A. Leibfarth, H. Sardon, *Nature* **2022**, *603*, 803.
[16] R. W. Clarke, T. Sandmeier, K. A. Franklin, D. Reich, X. Zhang, N. Vengallur, T. K. Patra, R. J. Tannenbaum, S. Adhikari, S. K. Kumar, T. Rovis, E. Y.-X. Chen, *Nature* **2023**, *616*, 731.
[17] M. Maaz, A. Riba-Bremerch, C. Guibert, N. J. Van Zee, R. Nicolaÿ, *Macromolecules* **2021**, *54*, 2213.
[18] M. Ahmadi, A. Hanifpour, S. Ghiassinejad, E. van Ruymbeke, *Chem. Mater.* **2022**, *34*, 10249.
[19] K. Yu, P. Taynton, W. Zhang, M. L. Dunn, H. J. Qi, *RSC Adv* **2014**, *4*, 10108.
[20] A. Durand-Silva, R. A. Smaldone, *ACS Cent. Sci.* **2020**, *6*, 836.
[21] D. T. Sheppard, K. Jin, L. S. Hamachi, W. Dean, D. J. Fortman, C. J. Ellison, W. R. Dichtel, *ACS Cent. Sci.* **2020**, *6*, 921.
[22] R. H. Aguirresarobe, S. Nevejans, B. Reck, L. Irusta, H. Sardon, J. M. Asua, N. Ballard, *Prog. Polym. Sci.* **2021**, *114*, 101362.
[23] A. Demongeot, R. Groote, H. Goossens, T. Hoeks, F. Tournilhac, L. Leibler, *Macromolecules* **2017**, *50*, 6117.

[24] N. J. Van Zee, R. Nicolaÿ, in *Macromol. Eng.* (Eds.: N. Hadjichristidis, Y. Gnanou, K. Matyjaszewski, M. Muthukumar), Wiley, **2022**, pp. 1–38.
[25] M. Röttger, T. Domenech, R. van der Weegen, A. Breuillac, R. Nicolaÿ, L. Leibler, *Science* **2017**, *356*, 62.
[26] A. Breuillac, A. Kassalias, R. Nicolaÿ, *Macromolecules* **2019**, *52*, 7102.
[27] C. Taplan, M. Guerre, J. M. Winne, F. E. Du Prez, *Mater. Horiz.* **2020**, *7*, 104.
[28] F. Caffy, R. Nicolaÿ, *Polym. Chem.* **2019**, *10*, 3107.
[29] A. Breuillac, F. Caffy, T. Vialon, R. Nicolaÿ, *Polym. Chem.* **2020**, *11*, 6479.
[30] L. Li, X. Chen, K. Jin, J. M. Torkelson, *Macromolecules* **2018**, *51*, 5537.
[31] J. J. Cash, T. Kubo, D. J. Dobbins, B. S. Sumerlin, *Polym. Chem.* **2018**, *9*, 2011.
[32] Y. Liu, Z. Tang, D. Wang, S. Wu, B. Guo, *J. Mater. Chem. A* **2019**, *7*, 26867.
[33] L. Wang, Y. Liu, N. Hao, Y. Qiao, W. Zeng, L. Wei, A. Du, *Polymer* **2023**, *265*, 125595.
[34] S. Yu, F. Li, S. Fang, X. Yin, S. Wu, Z. Tang, L. Zhang, B. Guo, *Macromolecules* **2022**, *55*, 3236.
[35] J. J. Lessard, G. M. Scheutz, S. H. Sung, K. A. Lantz, T. H. Epps, B. S. Sumerlin, *J. Am. Chem. Soc.* **2020**, *142*, 283.
[36] J. J. Lessard, K. A. Stewart, B. S. Sumerlin, *Macromolecules* **2022**, *55*, 10052.
[37] F. Van Lijsebetten, K. De Bruycker, Y. Spiesschaert, J. M. Winne, F. E. Du Prez, *Angew. Chem. Int. Ed.* **2022**, *61*, DOI 10.1002/anie.202113872.
[38] F. Van Lijsebetten, T. Debsharma, J. M. Winne, F. E. Du Prez, *Angew. Chem. Int. Ed.* **2022**, *61*, DOI 10.1002/anie.202210405.
[39] J. Brandrup, E. H. Immergut, E. A. Grulke, Eds., *Polymer Handbook, 4th Edition*, Wiley, New York ; Chichester, **2004**.
[40] D. J. Haloi, S. Ata, N. K. Singha, D. Jehnichen, B. Voit, *ACS Appl. Mater. Interfaces* **2012**, *4*, 4200.
[41] T. D. Jones, J. S. Schulze, C. W. Macosko, T. P. Lodge, *Macromolecules* **2003**, *36*, 7212.
[42] Z. Wang, Y. Gu, M. Ma, M. Chen, *Macromolecules* **2020**, *53*, 956.
[43] M. J. Folkes, P. S. Hope, Eds., *Polymer Blends and Alloys*, Blackie Academic & Professional, London ; New York, **1993**.
[44] J. Zhang, S. Ji, J. Song, T. P. Lodge, C. W. Macosko, *Macromolecules* **2010**, *43*, 7617.
[45] R. J. Roe, *Methods of X-Ray and Neutron Scattering in Polymer Science*, Oxford University Press, New York, **2000**.
[46] R. G. Ricarte, F. Tournilhac, L. Leibler, *Macromolecules* **2019**, *52*, 432.
[47] S. Lazzari, L. Nicoud, B. Jaquet, M. Lattuada, M. Morbidelli, *Adv. Colloid Interface Sci.* **2016**, *235*, 1.
[48] D. Wang, T. P. Russell, *Macromolecules* **2018**, *51*, 3.
[49] K. L. Brinker, A. H. Lebovitz, J. M. Torkelson, W. R. Burghardt, *J. Polym. Sci. Part B Polym. Phys.* **2005**, *43*, 3413.
[50] F. Lednicky, G. H. Michler, *J. Mater. Sci.* **1990**, *25*, 4549.
[51] R. G. Ricarte, F. Tournilhac, M. Cloître, L. Leibler, *Macromolecules* **2020**, *53*, 1852.
[52] M. Rubenstein, R. H. Colby, *Polymer Physics*, Oxford University Press, Oxford, **2003**.
[53] N. Ning, S. Li, H. Wu, H. Tian, P. Yao, G.-H. Hu, M. Tian, L. Zhang, *Prog. Polym. Sci.* **2018**, *79*, 61.

Georges J. M. Formon, Sonja Storch, Bruno Bresson, Nathan J. Van Zee*, and Renaud Nicolaÿ*

Overcoming the Tradeoff between Processability and Mechanical Performance of Elastomeric Vitrimers

Microphase-separated vitrimers prepared from incompatible hard/soft complementary thermoplastics via reactive extrusion break the paradigm of the tradeoff between processability and mechanical performance. The high-T_g dispersed phase reinforces the low-T_g major phase at service temperature, while crosslinking only within the interfacial regions enhances the material's ability to flow during processing at high temperature.

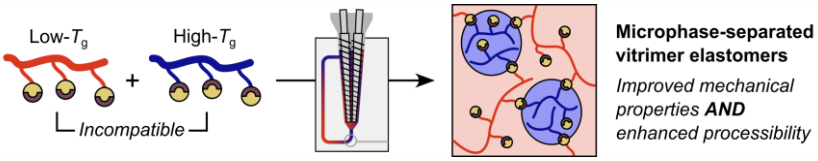

Supporting Information

Overcoming the Tradeoff between Processability and Mechanical Performance of Vitrimer Elastomers

Georges J. M. Formon[1], Sonja Storch[1], Arnaud Y.-G. Delplanque[1], Bruno Bresson[2], Nathan J. Van Zee[1], and Renaud Nicolaÿ[1]**

G. J. M. Formon, S. Storch, A. Y-G. Delplanque, N. J. Van Zee, R. Nicolaÿ
Chimie Moléculaire, Macromoléculaire, Matériaux (C3M), UMR7617, ESPCI Paris, Université PSL, CNRS, 75005 Paris, France
E-mail: nathan.van-zee@espci.psl.eu; renaud.nicolay@espci.psl.eu

Bruno Bresson
Sciences et Ingénierie de la Matière Molle (SIMM), UMR 7615, ESPCI Paris, Université PSL, CNRS, 75005 Paris, France

1. Materials and Methods

Materials. 1,2,6-Hexanetriol was purchased from TCI Chemicals. *N*,*N*-Diisopropylethylamine (DIPEA), 4-dimethylaminopyridine (DMAP), methacrylic anhydride, 1,2-propanediol, azobisisobutyronitrile (AIBN), 4-carboxyphenylboronic acid and 4-vinylbenzyl chloride were purchased from Sigma Aldrich. Methyl methacrylate (MMA), styrene, 2-ethylhexyl methacrylate (EHMA), magnesium sulfate anhydrous ($MgSO_4$), potassium carbonate (K_2CO_3) and anisole were purchased from Alfa Aesar. Phenylboronic acid and 1,4-phenylenediboronic acid were purchased from Combi-Blocks. Irganox 1010 was purchased from BASF. Ethyl acetate, tetrahydrofuran (THF), dichloromethane (DCM), dimethyl sulfoxide (DMSO), hexanes and acetone were purchased from Carlo Erba. Deuterated solvents were purchased from Eurositop. All reagents and solvents were used as received unless noted. MMA, styrene and EHMA were passed through a basic alumina column and stored in the freezer until utilization (−20 °C). AIBN was crystallized from methanol and stored in the freezer until utilization (−20 °C). 5,6-Dihydroxyhexyl methacrylate (see Figure S1 for the ^{1}H NMR spectrum) and (4-ethenylphenyl)methyl 4-(4-methyl-1,3,2-dioxaborolan-2-yl)benzoate (**StyBE**, see Figure S2

for the ^{1}H NMR spectrum) were synthesized by modified literature procedures,[S1,S2] which are fully described below. 2,2'-(1,4-Phenylene)-bis[4-methyl-1,3,2-dioxaborolane] (**BisBE**) was synthesized according to the literature procedure and spectra were consistent with what has been described.[S2]

Compression molding. Compression molding was performed in a Carver hot press using custom copper molds. To obtain specimens suitable for the different experiments, all samples were compression molded into 90 × 40 × 1.5 mm films at 220 °C and a pressure of 3 tons for 5 minutes for extruded samples and 10 minutes for vitrimers prepared in solution. Samples were then punched out using a die cutter of the desired shape, depending on application: 25 or 10 mm diameter disks for rheology; 40 × 5 mm rectangular bars for DMA; dog-bone shaped specimens according to ISO 527-2 type 5B for tensile testing.

Nuclear magnetic resonance (NMR) spectroscopy. ^{1}H and ^{13}CNMR spectra were recorded on a Bruker AVANCE 400 spectrometer at 296 K and frequencies of 400 and 101 MHz, respectively. The obtained spectra were referenced to the residual solvent peaks according to Fulmer et *al*.[S3]

Size exclusion chromatography (SEC). SEC was performed at 30 °C on a Viscotek GPCmax/VE2001 with THF as the elution solvent. The chromatograms were recorded with a triple detection array (TDA 305). Solvent flow rate was set to 1 mL/min and injection volumes were of 100 µL. Molar masses were calculated against a PMMA calibration curve using the refraction index signal.

Samples were dissolved in THF at a 1 mg/mL concentration with 10 µL of toluene per 10 mL of solution. 1,2 Propanediol was added to the solutions of the high-T_g polymer **H** to prevent boroxine formation during the analysis. For crosslinked materials, 50 µL of 1,2-propanediol were added per 10 mL of solution to decrosslink the samples prior to SEC analysis. All solutions were filtered through 0.2 µm polytetrafluoroethylene (PTFE) filters before injection.

Gel fraction determination. Samples were placed in $CHCl_3$ (approximately 10 mL for 100 mg of sample) for 24 h at room temperature. Solids were recovered by filtration through an aluminum woven stainless wire mesh and dried at room temperature for 24 h under air and then 24 h under vacuum at 120 °C. The dry gel (m_f) was then weighed and the value compared to the initial weight (m_i). Measurements were performed in triplicates. Gel fraction (%gel) was calculated according to the equation $\%gel = m_f/m_i \times 100\%$.

Tensile testing. Uniaxial tensile testing was performed with an Instron 5564 mounted with a 1 kN cell at room temperature. Measurements were performed according to ISO 527-2, with a displacement of 10 mm/min (corresponding to 100 %/min) in quintuplicates. Young's modulus

was calculated by taking the slope of the stress-strain curve between 0.25 and 5% strain. Toughness was obtained by calculating the area below the stress-strain curve.

Small-angle X-ray scattering (SAXS). SAXS measurements were performed at the SWING beamline at the SOLEIL Synchrotron Source. They were performed at a wavelength $\lambda = 1.03$ Å (E = 12 keV) and recorded at room temperature at a detector distance of 4 m to cover the scattering vector (q) range of 0.00156 to 0.237 $Å^{-1}$. Samples were cut-out into 5 mm diameter disks using a die cutter and placed inside aluminum washers to facilitate mounting the sample.

Atomic force microscopy (AFM). AFM was performed on a Bruker ICON AFM operated by a Nanoscope V controller. Measurements were conducted in tapping mode with a Budget Sensor Tap300 Probe (spring constant of 40 N/m), at 300 kHz frequency, free amplitude in the order of 10 nm and amplitude reduction of 0.9. The surface of the sample was analyzed after compression molding.

Scanning electron microscopy (SEM). SEM was performed using a Quattro ESEM from ThermoFischer Scientific with accelerating voltage of 5 kV and current of 1 nA. Samples were deposited on a conductive carbon tape and coated with a gold layer of around 5 nm using a Cressington 108 sputter coater at 20 mA for 30 s.

Samples were prepared either by cryogenic fracture or according to Lednicky and Michler,[S4] where samples are partially cut and fractured by pulling on each side with tweezers, both at room temperature and at 70 °C, although no significant difference has been observed for these temperatures. The fractured portion was then observed by SEM.

Image processing was performed using ImageJ[S5] by applying an automatic threshold selection using Otsu's clustering method[S6] and the internal ImageJ particle analyzer setting no threshold for ellipticity and a minimum area of 0.01 μm^2. The characteristic dimensions of the aggregates were calculated by taking the mean of the major and minor axes of each fitted ellipse. $\mathbf{Ext_{>75\mu m}}$ particles were counted and measured manually using the ellipse tool of ImageJ.

Thermogravimetric analysis (TGA). TGA was performed on a SETARAM Themys one under nitrogen flow. The samples (5 to 10 mg) were heated at a constant rate of 10 °C/min from 25 to 600 °C. For isotherms, the furnace was heated at a rate of 10 °C/min to 220 °C, and then this temperature was maintained for 30 min.

Differential scanning calorimetry (DSC). DSC was performed on a TA Instruments Q1000 under helium flow equipped with a liquid nitrogen external cooling accessory and calibrated using sapphire and high purity indium metal. Samples were prepared in hermetically sealed pans (5 to 10 mg) and were referenced to an empty pan. The typical heating and cooling ramps

were from −50 to 200 °C at 20 °C/min and back with a 2-minute hold at the highest and lowest temperatures.

Dynamic mechanical analysis (DMA). DMA were performed in a TA Instruments Q800 DMA in tension using rectangular specimens as described above. Measurements were performed with constant 1 % deformation and 1 Hz frequency, from −75 to 250 °C at a heating rate of 3 °C/min.

Rheology. Rheology was performed with an Anton Paar MCR 501 rheometer under nitrogen flow (100 L/h) using a 25 mm diameter plate-plate geometry and a constant normal force of F_N=0.1 N to ensure contact throughout the experiment. Small amplitude oscillatory shear frequency sweeps were performed under constant deformation of γ=1%. Creep and recovery experiments were performed with variable stresses (depending on the temperature) with 30 minutes of creep and 30 minutes of recovery. Creep was performed four times for each temperature or until the curves were superimposed, whichever comes first. Amplitude sweeps were performed at a constant angular frequency of ω=1 rad/s. When multiple temperatures were used, the samples were equilibrated for 10 minutes at each temperature before the experiment. Creep experiments at 10 kPa and 30 °C were performed with Anton Paar MCR 302 or MCR 302e rheometers under air.

Calculation of the conversion of the dioxaborolane metathesis. If we consider dioxaborolane metathesis as a degenerate chemical reaction and that the dioxaborolanes in **S** (S_{BE}) and in **H** (H_{BE}) present the same reactivity, the equilibrium constant of the reaction below should be equal to 1:[S2]

$$S_{BE} + H_{BE} \rightleftharpoons C + BE$$

$$\frac{[C][BE]}{[S_{BE}][H_{BE}]} = 1$$

Where C and BE are respectively crosslinks and the free dioxaborolane that is released.[S2] We know from the compositions of **H** and **S** that the initial molar ratio of dioxaborolanes originating from the two polymers is equal to 3.4 ($S_{BE}^0/H_{BE}^0 = 3.4$). If we consider that initially there are no crosslinks nor free dioxaborolanes ($C^0 = BE^0 = 0$), the content of C and BE will be equal to the extent of reaction ($[C] = [BE] = \xi$). At equilibrium, we should have:

$$\frac{\xi^2}{(S_{BE}^0 - \xi)(H_{BE}^0 - \xi)} = 1$$

$$\xi^2 = S_{BE}^0 \times H_{BE}^0 - (S_{BE}^0 + H_{BE}^0) \times \xi + \xi^2$$

$$\xi = \frac{S_{BE}^0 \times H_{BE}^0}{S_{BE}^0 + H_{BE}^0}$$

The conversion (X) is equal to the extent of reaction (ξ) divided by the initial content of the limiting reactant (H_{BE}^0).

$$X = \frac{\xi}{H_{BE}^0} = \frac{S_{BE}^0}{S_{BE}^0 + H_{BE}^0} = \frac{S_{BE}^0/H_{BE}^0}{(S_{BE}^0 + H_{BE}^0)/H_{BE}^0} = \frac{S_{BE}^0/H_{BE}^0}{S_{BE}^0/H_{BE}^0 + 1} = \frac{3.4}{4.4} = 0.77$$

To calculate the conversion of the dioxaborolanes in **S** (X_S):

$$X_S = \frac{\xi}{S_{BE}^0} = \frac{H_{BE}^0}{S_{BE}^0 + H_{BE}^0} = \frac{H_{BE}^0/S_{BE}^0}{H_{BE}^0/S_{BE}^0 + 1} = \frac{1/3.4}{1/3.4 + 1} = 0.23$$

2. Synthesis

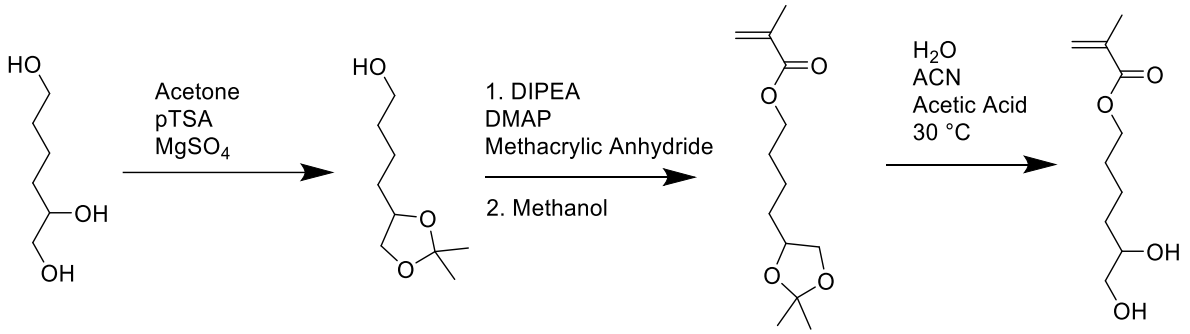

4-(2,2-Dimethyl-1,3-dioxolan-4-yl)butan-1-ol. 1,2,6-Hexanetriol (31 g, 234 mmol) was dissolved in acetone (500 mL) in the presence of anhydrous magnesium sulfate (56 g, 465 mmol). Para-toluene sulfonic acid (3.8 g, 20 mmol) was slowly added and the mixture was stirred at room temperature. After 24 hours sodium bicarbonate (3.4 g, 40 mmol) was added and stirring was continued for 3 h at room temperature. The mixture was filtered and concentrated under reduced pressure. Water (350 mL) was added and the organic phase was extracted with dichloromethane (DCM) (3 x 200 mL). The organic phase was dried over $MgSO_4$, filtered, and concentrated under reduced pressure to obtain a transparent liquid (21 g, 51%). Characterization by NMR spectroscopy matched the previously reported spectral data.[S1,S2] ^{1}H NMR (400 MHz, DMSO) δ 4.35 (t, *J* = 5.2 Hz, 1H), 4.05 – 3.87 (m, 2H), 3.47 – 3.34 (m, 3H), 1.57 – 1.31 (m, 6H), 1.27 (d, *J* = 17.9 Hz, 6H). ^{13}C NMR (101 MHz, $CDCl_3$) δ 108.83, 76.14, 69.56, 62.78, 33.38, 32.73, 27.06, 25.85, 22.17.

4-(2,2-Dimethyl-1,3-dioxolan-4-yl)butyl methacrylate. 4-(2,2-Dimethyl-1,3-dioxolan-4-yl)butan-1-ol (37.6 g, 216 mmol), N,N-diisopropylethylamine (41 mL, 238 mmol), 4-dimethylaminopyridine (260 mg, 2.2 mmol) and methacrylic anhydride (35 mL, 238 mmol) were mixed and stirred for 24 h at room temperature. Methanol (9 mL) was added and the

mixture was stirred for additional 3 hours. Hexanes (200 mL) was added and the organic phase was washed with water (1x 100 mL), 0.5 M HCl (3 x 100 mL), 0.5 M NaOH (3 x 100mL), water (1 x 100mL) and brine (1 x 100mL). The organic phase was dried over MgSO4, filtered, and concentrated under reduced pressure at 25 °C to obtain a slightly yellow liquid (44 g, 84%). Characterization by NMR spectroscopy matched the previously reported spectral data.[S1,S2] ^{1}H NMR (400 MHz, DMSO) δ 6.01 (dd, *J* = 1.7, 0.9 Hz, 1H), 5.67 (p, *J* = 1.5 Hz, 1H), 4.18 – 3.93 (m, 4H), 3.41 (t, *J* = 7.0 Hz, 1H), 1.90 – 1.85 (m, 3H), 1.69 – 1.20 (m, 12H). ^{13}C NMR (101 MHz, $CDCl_3$) δ 167.64, 136.58, 125.44, 108.90, 76.01, 69.54, 64.59, 33.34, 28.76, 27.08, 25.86, 22.47, 18.47.

5,6-Dihydroxyhexyl methacrylate. 4-(2,2-dimethyl-1,3-dioxolan-4-yl)butyl methacrylate (11.8 g, 48.7 mmol) was dissolved in a 1:1 mixture of water and acetonitrile (140 mL). Acetic acid (6.5 mL, 114 mmol) was added and the mixture was stirred for 24h at 30 °C with N_2 bubbling. The mixture, which was initially turbid, became translucid and was added to a separatory funnel and extracted with ethyl acetate (6 x 40 mL). The combined organic phases were then washed with NaOH 0.5 M (5 x 40 mL), water (3 x 30 mL) and brine (1 x 30 mL). The organic phase was dried over $MgSO_4$ and solvent was removed under reduced pressure at 25 °C. A viscous yellowish liquid was obtained (6.86 g, 70%). Characterization by NMR spectroscopy matched the previously reported spectral data.[S1,S2] ^{1}H NMR (400 MHz, $CDCl_3$) δ 6.08 (s, 1H), 5.54 (s, 1H), 4.14 (t, *J* = 6.6 Hz, 2H), 3.78 – 3.55 (m, 2H), 3.52 – 3.33 (m, 1H), 2.80 – 2.43 (b, 2H), 1.93 (s, 3H), 1.78 – 1.63 (m, 2H), 1.60 – 1.31 (m, 4H). ^{13}C NMR (101 MHz, $CDCl_3$) δ 167.75, 136.51, 125.55, 72.15, 66.85, 64.62, 32.73, 28.72, 22.17, 18.43.

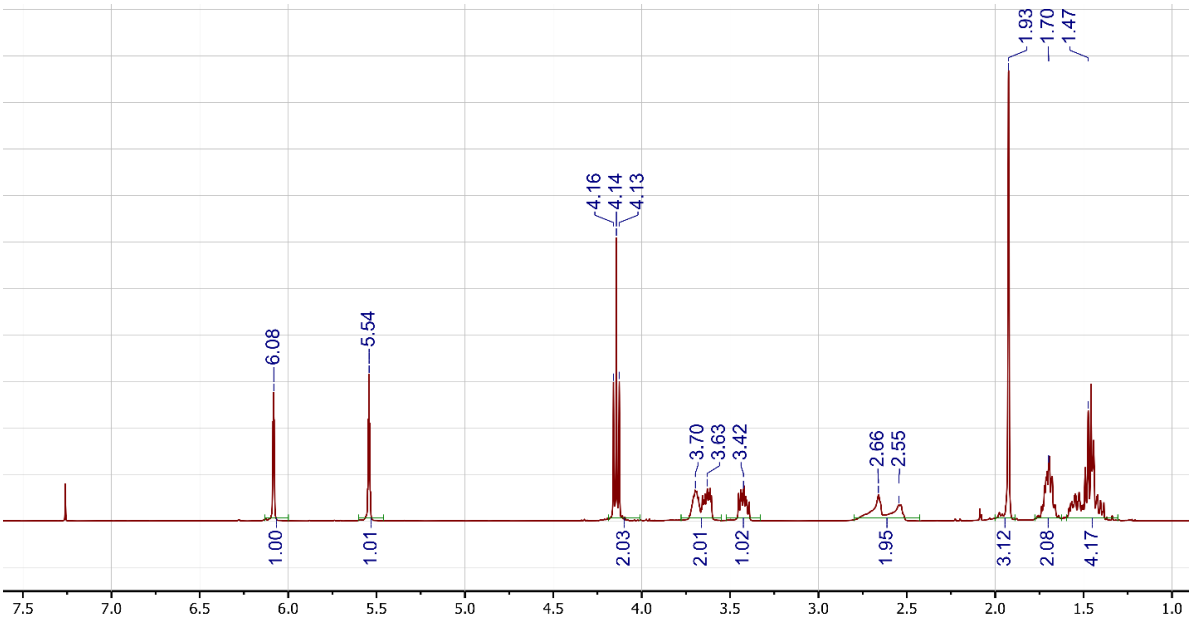

Figure S1. ^{1}H NMR spectrum of 5,6-dihydroxyhexyl methacrylate in $CDCl_3$ at 296 K.

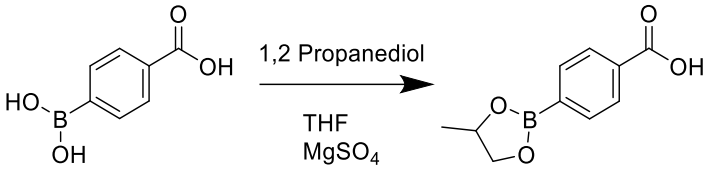

4-(4-Methyl-1,3,2-dioxaborolan-2-yl)benzoic acid. 4-Carboxy phenyl boronic acid (10 g, 60 mmol) and 1,2 propanediol (4.4 mL, 60 mmol) were suspended in acetone (300 mL). Water was added (1 mL) and the suspension was stirred until complete dissolution (around 3 hours). Magnesium sulfate (30 g, 250 mmol) was added in six portions spaced by 30 minutes and the mixture was further reacted for 18 hours. After that, $MgSO_4$ was filtered off and the solvent was removed under reduced pressure, yielding an off-white powder (11.75 g, 95%). Characterization by NMR spectroscopy matched the previously reported spectral data.[S1] ^{1}H NMR (400 MHz, DMSO) δ 13.09 (s, 1H), 7.96 (d, *J* = 8.1 Hz, 2H), 7.81 (d, *J* = 8.1 Hz, 2H), 4.74 (h, *J* = 6.3 Hz, 1H), 4.58 – 4.35 (m, 1H), 3.87 (dd, *J* = 8.9, 7.3 Hz, 1H), 1.34 (d, *J* = 6.2 Hz, 3H). ^{13}C NMR (101 MHz, DMSO) δ 167.65, 135.02, 129.06, 74.15, 72.56, 21.96. Carbon adjacent to boron could not be detected.

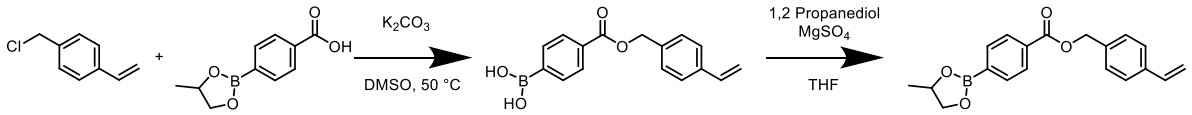

(4-Ethenylphenyl)methyl 4-(4-methyl-1,3,2-dioxaborolan-2-yl)benzoate (StyBE). 4-(4-methyl-1,3,2-dioxaborolan-2-yl)benzoic acid (3.6 g, 17.5 mmol) and potassium carbonate (4.84 g, 35 mmol) were dissolved in DMSO (100 mL). After complete dissolution, 4-(Chloro methyl) styrene (2.2 mL, 15.7 mmol) was slowly added and the mixture was stirred at 50 °C for 48 hours under nitrogen atmosphere. The solution was then poured into water (500 mL) and extracted with ethyl acetate (6 x 100 mL). The organic phase was washed with water (3 x 125 mL), dried with anhydrous $MgSO_4$ and solvent was removed under reduced pressure yielding a sticky oil. The obtained boronic acid (2.90 g, 10 mmol) was then stirred in THF (20 mL) with 1,2 propanediol (0.75 mL, 10 mmol) and water (0.1 mL) until complete dissolution. Anhydrous magnesium sulfate was then added (7.2 g, 60 mmol) in six batches and the suspension was stirred overnight. The solids were removed *via* filtration and solvents were removed under reduced pressure, yielding a pasty light brown solid (2.13g, 42% over two steps). Characterization by NMR spectroscopy matched the previously reported spectral data.[S1] ^{1}H NMR (400 MHz, $CDCl_3$) δ 8.06 (d, *J* = 8.2 Hz, 2H), 7.87 (d, *J* = 8.3 Hz, 2H), 7.43 (d, *J* = 2.1 Hz, 4H), 6.73 (dd, *J* = 17.6, 10.9 Hz, 1H), 5.77 (dd, *J* = 17.6, 0.9 Hz, 1H), 5.35 (s, 2H), 5.27 (dd, *J* = 10.9, 0.9 Hz, 1H), 4.75 (td, *J* = 7.5, 6.2 Hz, 1H), 4.48 (dd, *J* = 8.9, 7.7 Hz, 1H), 3.91

(dd, J = 8.9, 7.3 Hz, 1H), 1.43 (d, J = 6.3 Hz, 3H). ^{13}C NMR (101 MHz, $CDCl_3$) δ 166.43, 137.68, 136.35, 135.43, 134.75, 132.45, 128.83, 128.55, 126.44, 114.38, 74.07, 72.72, 66.60, 21.77. Carbon adjacent to boron could not be detected.

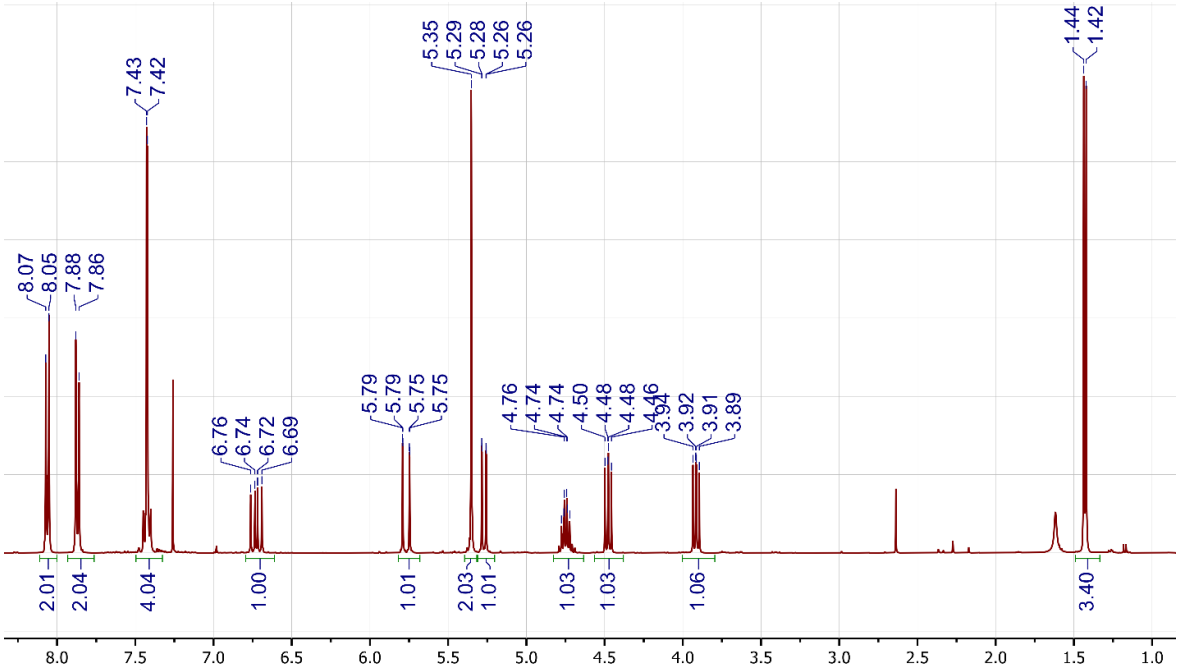

Figure S2. ^{1}H NMR spectrum of **StyBE** in $CDCl_3$ at 296 K.

Synthesis of low-T_g polymer (S). EHMA (71.8 g, 362 mmol), 5,6-dihydroxyhexyl methacrylate (5.00 g, 24.7 mmol), styrene (3.67 g, 35.3 mmol) and anisole (90 mL) were placed in a Schlenk flask with AIBN (21.6 mg, 0.132 mmol), which was introduced as a solution in DMF (19.5 mg/mL). The solution was degassed by bubbling at least 30 min with nitrogen gas. After that, an aliquot of the reaction mixture was taken to evaluate the initial composition by ^{1}H NMR, which was found to be 5.9/85.8/8.4 for 5,6-dihydroxyhexyl methacrylate/EHMA/styrene. The reactor was then sealed and placed for 25.5 h in an oil bath thermostated at 65 °C, until styrene reached a conversion of 76% and methacrylates 55%, calculated by comparing the initial and final integrals of the vinyl peaks of the monomers based on ^{1}H NMR spectroscopy using DMF as internal standard. The polymer was precipitated twice into methanol, filtered and dried at 120 °C under vacuum for 18 h. From the conversion of the monomers (calculated by ^{1}H NMR), it was determined that the polymer contained 5.7 mol% of 5,6-dihydroxyhexyl methacrylate, 11.3 mol% of styrene and an average repeating unit molar mass of 187.9 g/mol, which was confirmed by the NMR spectrum of the dried polymer (Figure S3).

The resulting polymer (44 g, 13.3 mmol of diols) was then solubilized in toluene with phenylboronic acid (1.63 g, 13.3 mmol) and water (10 mL). The reaction mixture was refluxed for 8 hours in a Dean-Stark apparatus. The polymer was precipitated twice in acetonitrile and

dried under high vacuum at 120 °C for 18 h to afford **S** (44 g, 96% yield over two steps, based on monomers conversion) as a soft transparent solid. The calculated average repeating unit molar mass was 192.8 g/mol. The ^{1}H NMR spectrum of **S** can be found in Figure. S3. From size exclusion chromatography (SEC) in THF (Figure S6a), it was found M_n=421 kg/mol with $Đ$=1.99 (conventional calibration with PMMA standards). T_g was found to be 5 °C by differential scanning calorimetry (Figure S7a). Thermogravimetric analysis (TGA) shows no degradation of **S** below 250 °C (Figure S8a).

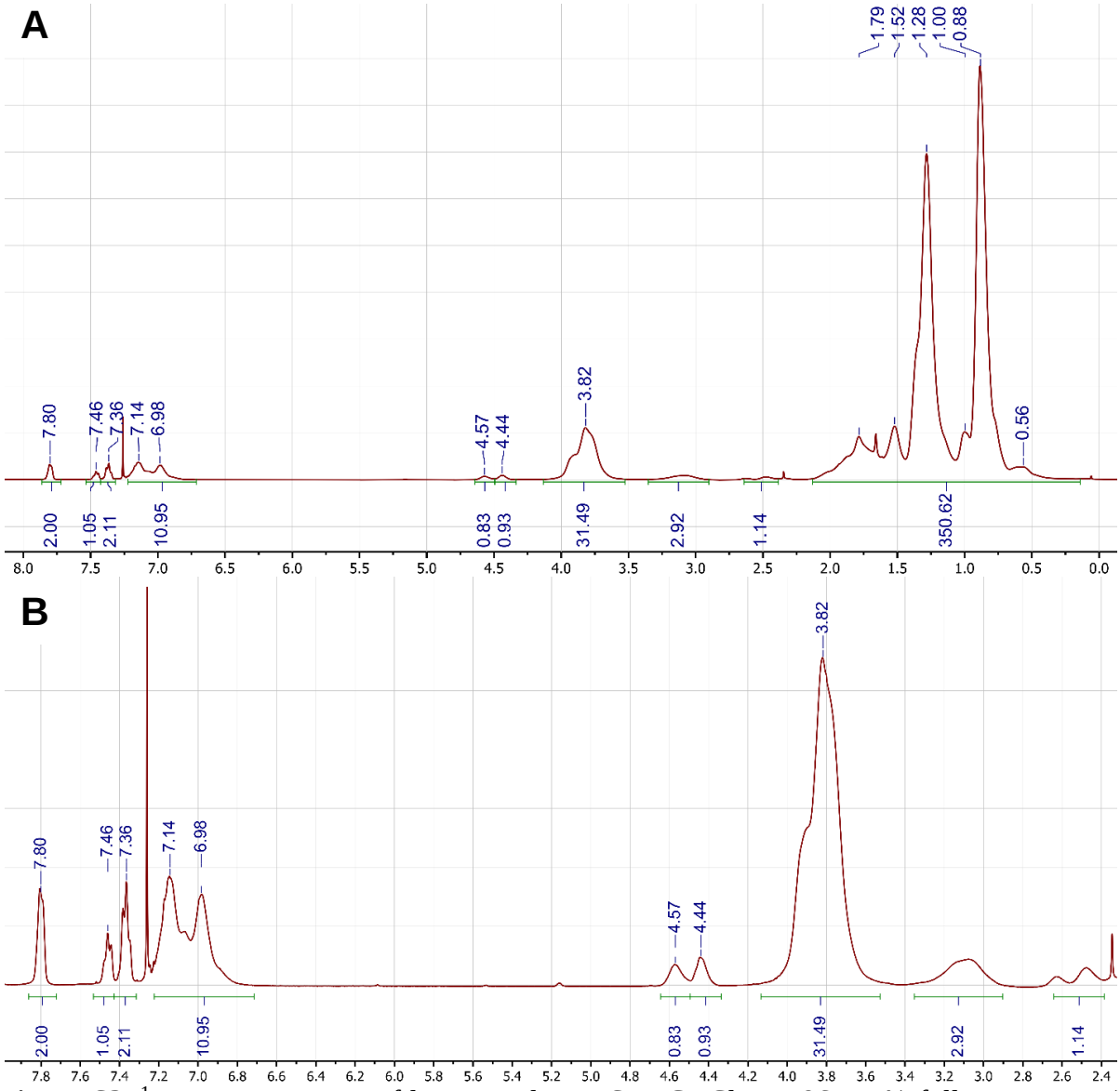

Figure S3. ^{1}H NMR spectrum of low-T_g polymer **S** in $CDCl_3$ at 296 K. A) full spectrum. B) zoomed in view of the 2.4–8.0 ppm region.

Synthesis of high-T_g polymer (H). MMA (20.7 g, 207 mmol), **StyBE** (6.01 g, containing 5.6 wt% 1,2 propanediol, which translates to 5.67 g, 17.6 mmol of monomer) and anisole (20 mL) were placed in a Schlenk tube with AIBN (157 mg, 0.959 mmol), which was introduced as a

solution in DMF (19.5 mg/mL). The solution was degassed by bubbling at least 30 minutes with nitrogen gas. After that, an aliquot of the reaction mixture was taken to evaluate the initial composition by ^{1}H NMR, which was found to be 7.8/92.2 for **StyBE**/MMA. The reactor was then sealed and placed for 1.42 h in an oil bath thermostated at 80 °C, until **StyBE** reached a conversion of 89% and MMA 72% calculated by comparing the initial and final integrals of the vinyl peaks of the monomers based on ^{1}H NMR spectroscopy using DMF as internal standard. The polymer was precipitated twice into diethyl ether, the resulting suspension was filtered and the solids were dried at 120 °C under vacuum for 18 h, yielding **H** as a yellow powder (19.5 g, 97% yield). From the conversion of the monomers (calculated by ^{1}H NMR) it was determined that the polymer contained 9.5 mol% of **StyBE** and an average repeating unit molar mass of 121.2 g/mol, which was confirmed by the NMR spectrum of the dried polymer (Figure S4). By THF SEC, it was found that the final polymer had M_n=44.3 kg/mol and $Đ$=1.90 (Figure S6a). T_g was found to be 122 °C by DSC (Figure S7a), TGA shows no degradation of **H** below 250 °C (Figure S8b).

To be used in further experiments, **H** was cryogenically ground and passed through a 75 µm sieve, thus obtaining a batch of particles smaller than 75 µm (used for the synthesis of **Ext$_{<75µm}$**) and one larger than that (used for the synthesis of **Ext$_{>75µm}$**).

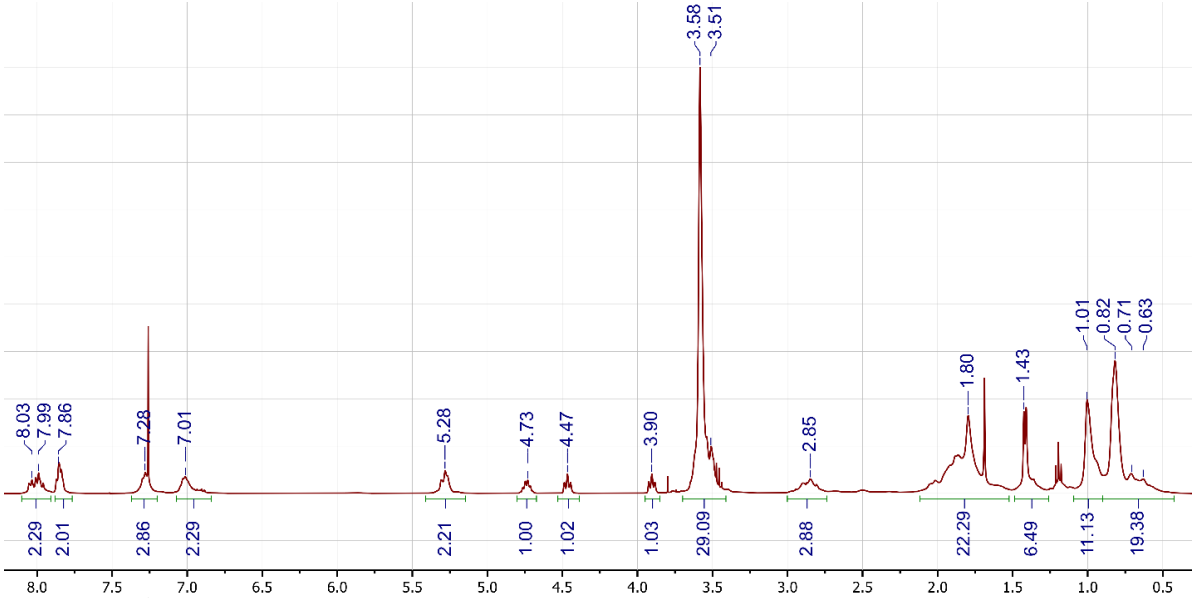

Figure S4. ^{1}H NMR spectrum of high-T_g polymer **H** in $CDCl_3$ at 296 K.

Preparation of a vitrimer via crosslinking with a bis(boronic ester) (BisBE Vit). Polymer **S** (2.04 g, 0.601 mmol of boronic ester) was dissolved in 10 mL DCM. Irganox 1010 stabilizer (20 mg) and **BisBE** (219 mg, 0.089 mmol) were added, and after 1 h the solution gelled. After 12 h, the gel was dried in air at room temperature for 24 h and then under vacuum at 150 °C for

18 h, obtaining **BisBEVit** as a light-yellow solid. Thermogravimetric analysis shows similar thermal stability as **S** (Figure S8c).

Synthesis of polymer-polymer vitrimer (Vit_{sol}). Polymer **S** (5.4 g, 1.59 mmol of boronic ester) was dissolved in 20 mL DCM with Irganox 1010 stabilizer (60 mg). In a different vial, **H** (600 mg, 0.471 mmol of boronic ester) was dissolved in 3 mL DCM. Both solutions were combined and the mixture gelled after 5 min. After 12 h, the gel was left to dry in air at room temperature for 24 h and then under vacuum at 150 °C for 18 h, obtaining $\mathbf{Vit_{sol}}$ as a light-yellow solid. Thermogravimetric analysis shows similar thermal stability as **S** (Figure S8d).

Preparation of vitrimers by reactive extrusion. All extrusions were performed using a 5 cc DSM Xplore batch twin-screw micro-compounder with nitrogen purging. A representative procedure for preparing $\mathbf{Ext_{<75\mu m}}$ is as follows. **S** (2.7 g , 0.80 mmol of boronic ester), **H** (300 mg, 0.24 mmol of boronic ester, particle size less than 75 µm) and Irganox 1010 (30 mg) were gradually introduced in the extruder at 140 °C with a screw speed of 50 rpm. After loading all of the material, the screw speed was increased to 200 rpm at the same temperature for 5 minutes. The temperature was then increased to 220 °C, at a rate of around 40 °C/min, and maintained for 10 minutes, after which the material was extruded and collected, yielding $\mathbf{Ext_{<75\mu m}}$ as a turbid light yellow soft solid. $\mathbf{Ext_{>75\mu m}}$ was synthesized following the same extrusion protocol as $\mathbf{Ext_{<75\mu m}}$ but using **H** particles with a size greater than 75 µm. Thermogravimetric analysis shows similar thermal stability as **S** (Figure S8e and S8f).

3. Simulation of the compositional drift in the synthesis of polymer H

Given radical copolymerizations of styrene-based monomers and methacrylates can lead to a drift of composition,[S7] we performed numerical simulations to gain insight into the compositional drift during the synthesis of **H.** O'Driscoll and co-workers[8] have previously shown that the integrated Mayo-Lewis equation (also known as the Meyer-Lowery equation) can be used to reasonably describe the copolymerization of styrene and methyl methacrylate up to high conversion. Following their application of the model, we found that the reactivity ratios r_{St}=0.60 and r_{MMA}=0.35 closely match the experimental data for the polymerization of **StyBE** with MMA with an initial monomer feed of f_{St}=0.078 and f_{MMA}=0.912 (Figure S5).

At a degree of conversion of 0.74 (i.e., the same total monomer conversion calculated based on ^{1}H NMR spectroscopy as described above), we calculated f_{St}=0.010, which corresponds to a conversion of 87% styrene (which is close to the experimental converion of **StyBE** of 89%). The instantaneous copolymer composition (F_{St}) at this degree of conversion is 2.0 mol%.

Finally, again at a degree of conversion of 0.77, the cumulative average for copolymer composition is 7.5 mol%, which is reasonably close to the experimentally determined value of 9.5 mol%. Given the heterogeneous nature of the present system, we judged that this degree of compositional drift would not lead to unintentional phase separation or dominate the viscoelastic response of our system.

Furthermore, we compared the refractive index and UV SEC traces (Figure S6c and d). Since the methacrylate monomers do not absorb strongly at 254 nm, the UV traces are selective for detecting the aromatic groups of styrene and the dioxaborolane-functionalized monomers. Gratifyingly, we see that the shape of the normalized RI and UV traces closely match with each other for both **S** and **H**, indicating that there was not a large fraction of chains without incorporation of the dioxaborolane-functionalized monomer in either material.

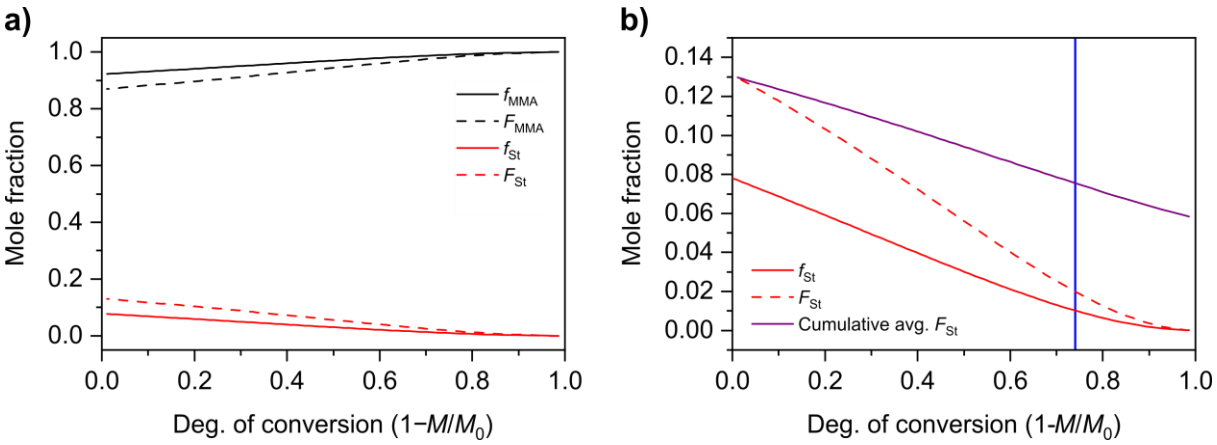

Figure S5. a) Simulated plot for the variation in the monomer feed (f_{St} and f_{MMA}) and copolymer composition (F_{st} and F_{MMA}) with conversion (where M is the moles of consumed monomer and M_0 is the initial total moles of monomer) for styrene (St) and methyl methacrylate (MMA). These plots were generated with the integrated Meyer-Lowry equation assuming $f_{St,0}$=0.078, $f_{MMA,0}$=0.922, r_{St}=0.60, and r_{MMA}=0.35. b) Zoomed view of the f_{St} and F_{St} curves with a cumulative average of F_{St}. The vertical blue line is at a degree of conversion of 0.74.

4. Size Exclusion Chromatography (SEC)

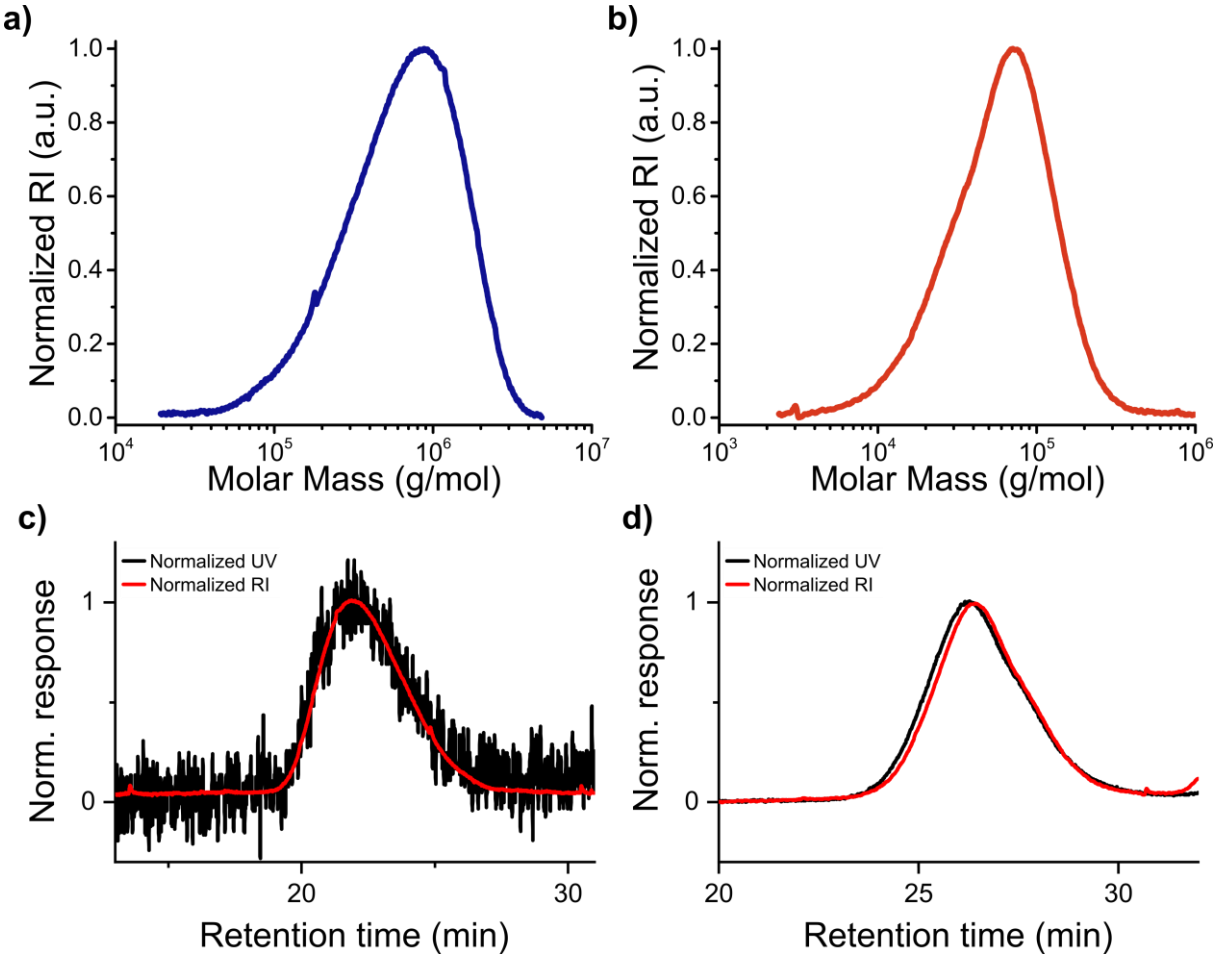

Figure S6. THF-SEC trace, normalized refractive index as a function of molar mass, of a) **S** and b) **H** with addition of 1,2-propanediol. Comparison of the normalized refractive index and UV traces (254 nm) as a function of retention time for c) **S** and d) **H** with addition of 1,2-propanediol.

5. Differential Scanning Calorimetry (DSC)

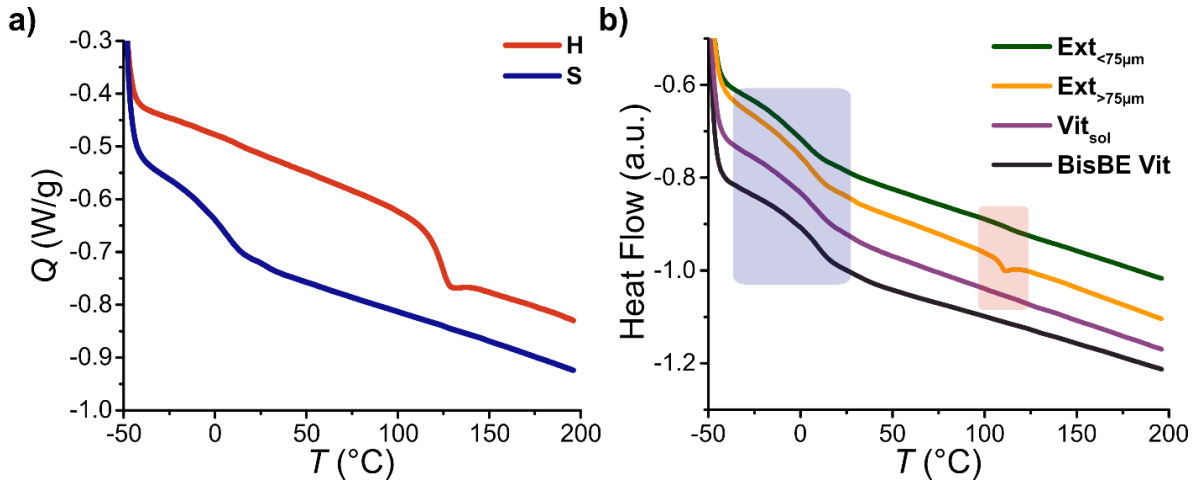

Figure S7. DSC trace of a) **H** and **S**; and b) **Ext_{<75µm}, Ext_{>75µm}, Vit_{sol}** and **BisBE Vit**. The blue and red rectangles represent the regions of the glass transition for **S** and **H** respectively. Curves have been vertically shifted to simplify comparison. For all samples, only the second heating curves are depicted (20 °C/min).

Table S1. Glass transition temperatures obtained from the DSC second heating curve.

Sample	T_g 1 (°C)	T_g 2 (°C)
S	5.2	n.a.[a]
H	n.a.[a]	122
Ext_{<75µm}	2.2	113
Ext_{>75µm}	3.6	109
Vit_{sol}	7.9	123
BisBE Vit	7.3	n.d.[b]

[a]Not applicable. [b]Not detected.

6. Thermogravimetric Analysis (TGA)

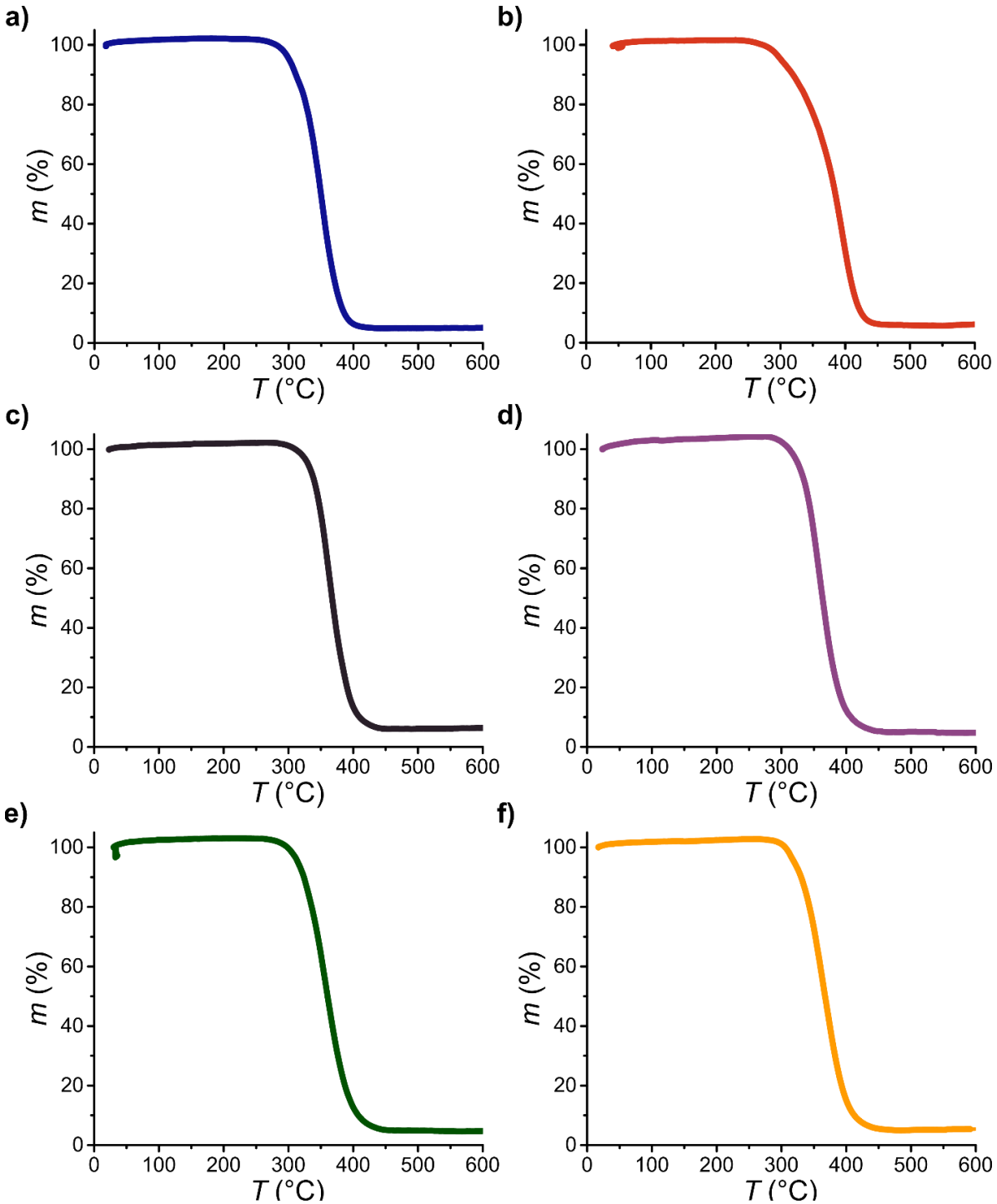

Figure S8. TGA trace of a) **S**, b) **H**, c) **BisBE Vit**, d) **Vit$_{sol}$**, e) **Ext$_{<75µm}$**, and f) **Ext$_{>75µm}$**. A heating rate of 10 °C/min was applied under N_2 flow.

7. Thermomechanical characterization of thermoplastic precursors

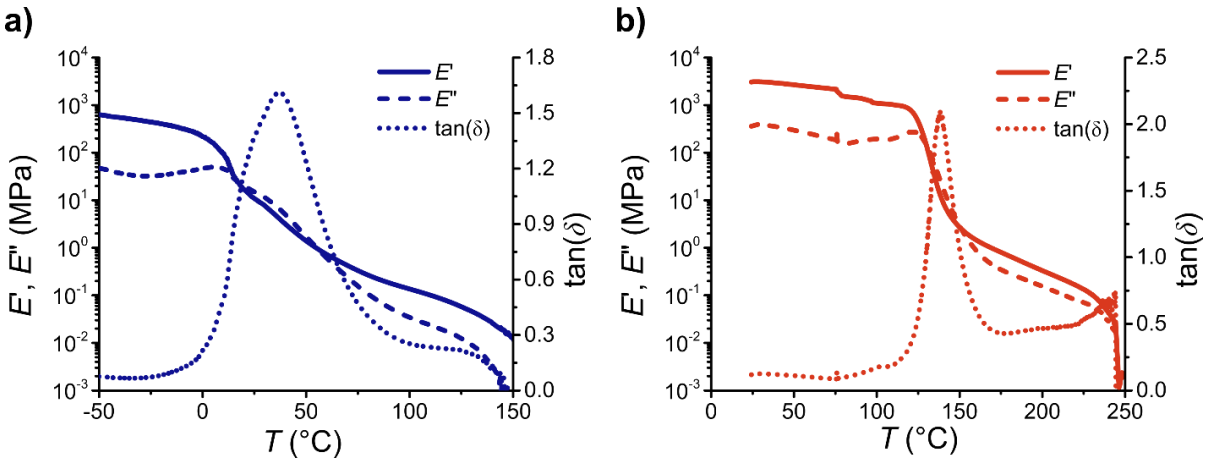

Figure S9. DMA traces of a) **S** and b) **H**. The left axis shows elongation storage and loss moduli. Loss factor is represented on the right axis.

Table S2. Glass transition temperatures obtained from the DMA tan(δ) and *E*" peaks.

Sample	tan(δ) peak		*E*" peak	
	T_g 1 (°C)	T_g 2 (°C)	T_g 1 (°C)	T_g 2 (°C)
S	37		6	
H		138		122

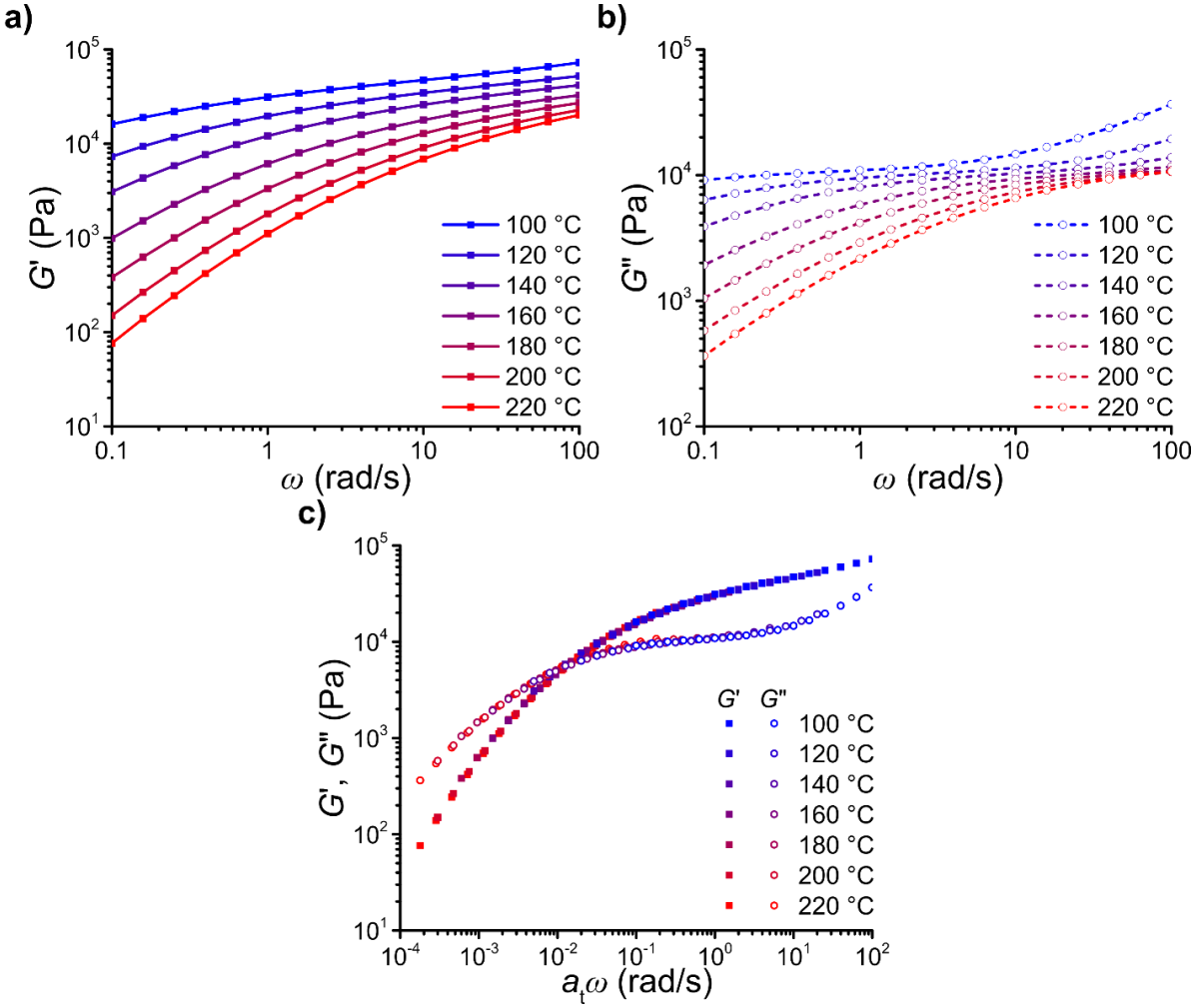

Figure S10. Multi-temperature frequency sweeps for **S**. a) Shear storage modulus (*G*') as a function of frequency. b) Shear loss modulus (*G*") as a function of frequency. c) Time-temperature superposition (TTS) of data in a) and b). Only horizontal shift factor was applied and the reference temperature is set to 100 °C.

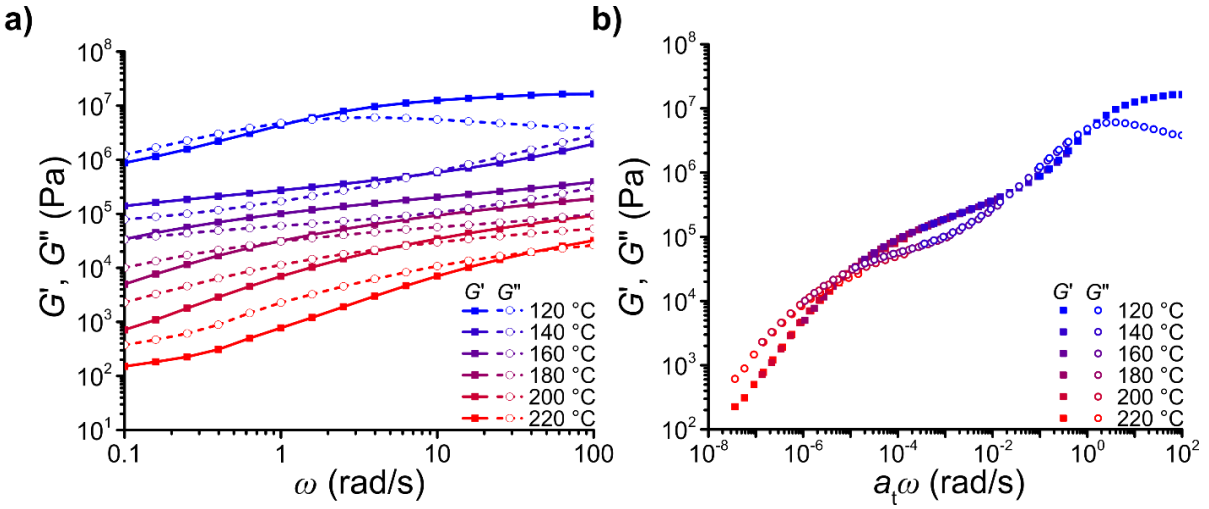

Figure S11. a) Multi-temperature frequency sweeps for **H**. Shear storage (*G*') and loss (*G*") moduli as a function of frequency. b) Time-temperature superposition (TTS) of data in a). Only horizontal shift factor was applied and the reference temperature is set to 120 °C.

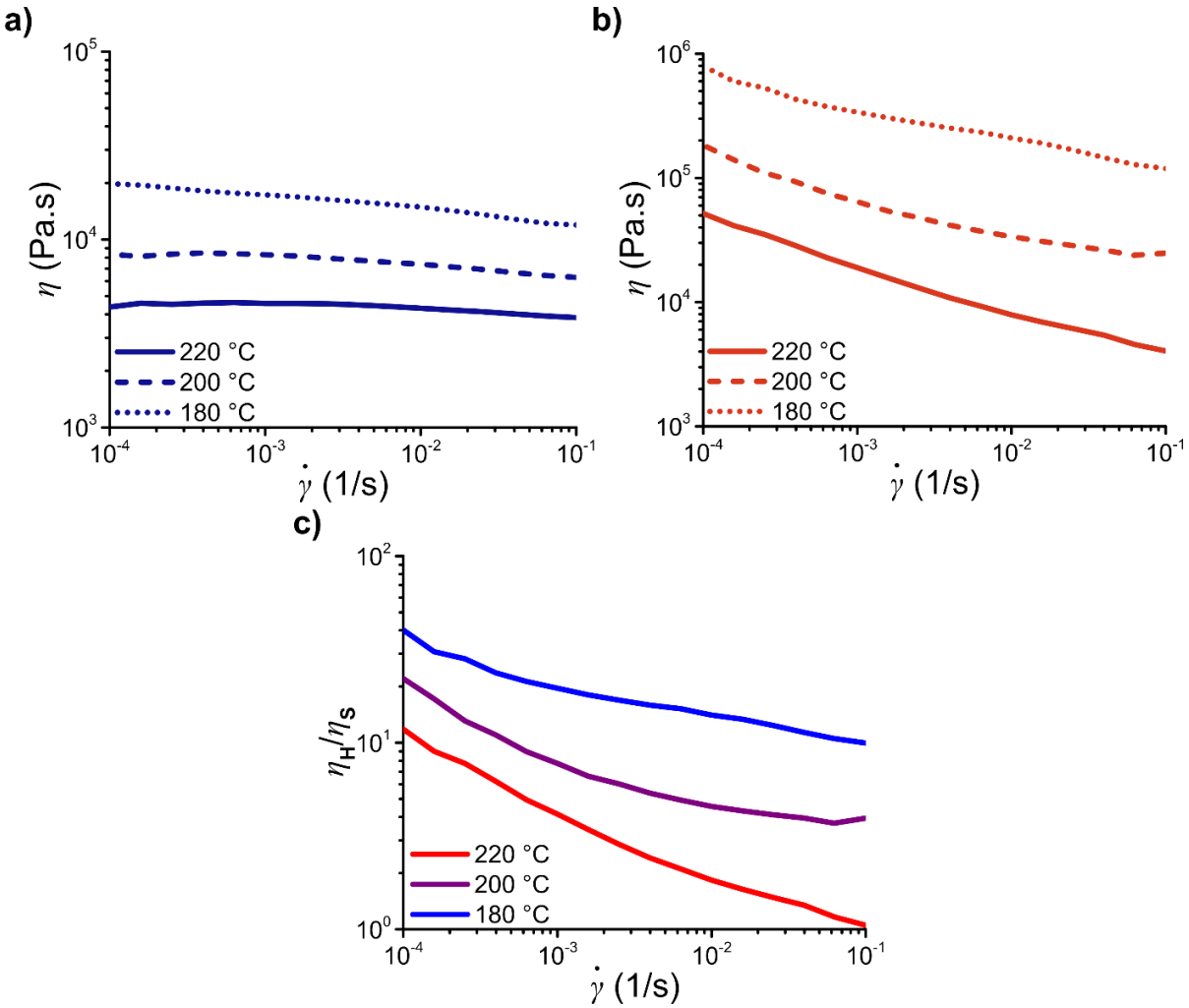

Figure 12. Flow curves, viscosity as a function of shear rate, of a) **S** and b) **H**. c) Viscosity ratio of **H** and **S** as a function of shear rate for 220, 200 and 180 °C.

8. Extrusion

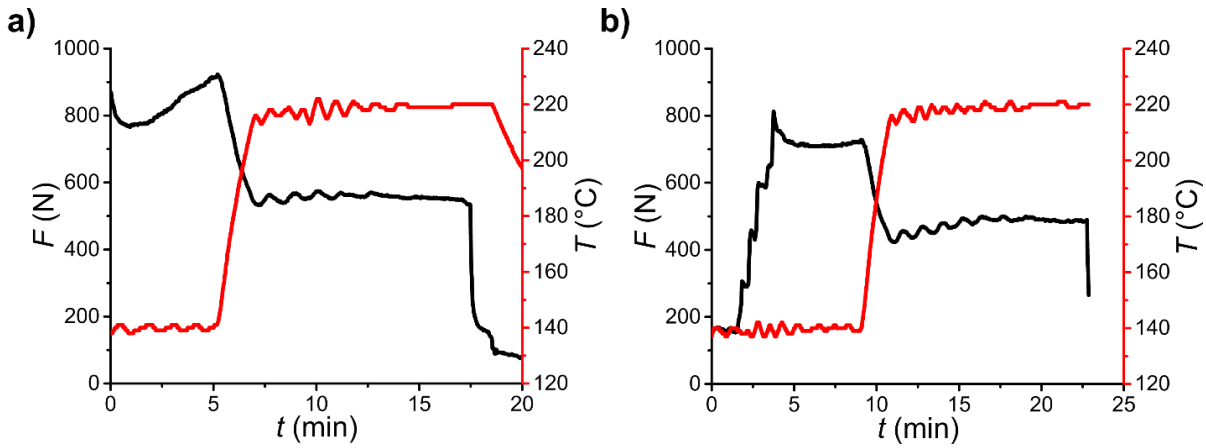

Figure S13. Representative extrusion profiles, force exerted by the extruder screws (left axis) and temperature (right axis) as a function of time, of a) **Ext**$_{<75\mu m}$ and b) **Ext**$_{>75\mu m}$.

9. Morphological analysis of vitrimers

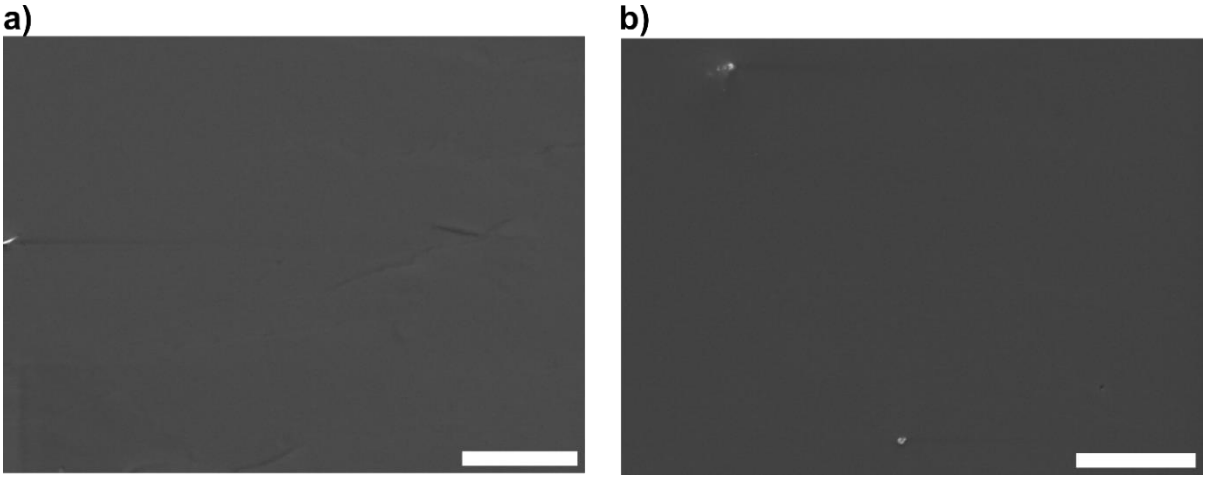

Figure S14. SEM of a) cryogenically fractured and b) soft fractured **BisBE Vit** surfaces. The scale bars are 10 µm**.**

Figure S15. Photographs of samples just above ESPCI logo (top row) and at 1 cm height (bottom row). From left to right: **S**, **Ext**$_{<75\mu m}$, **Ext**$_{>75\mu m}$, **Vit**$_{sol}$ and **BisBE Vit**. Yellowish color comes from **H** that is yellow and possibly from the degradation products of antioxidant used (Irganox 1010).[S11]

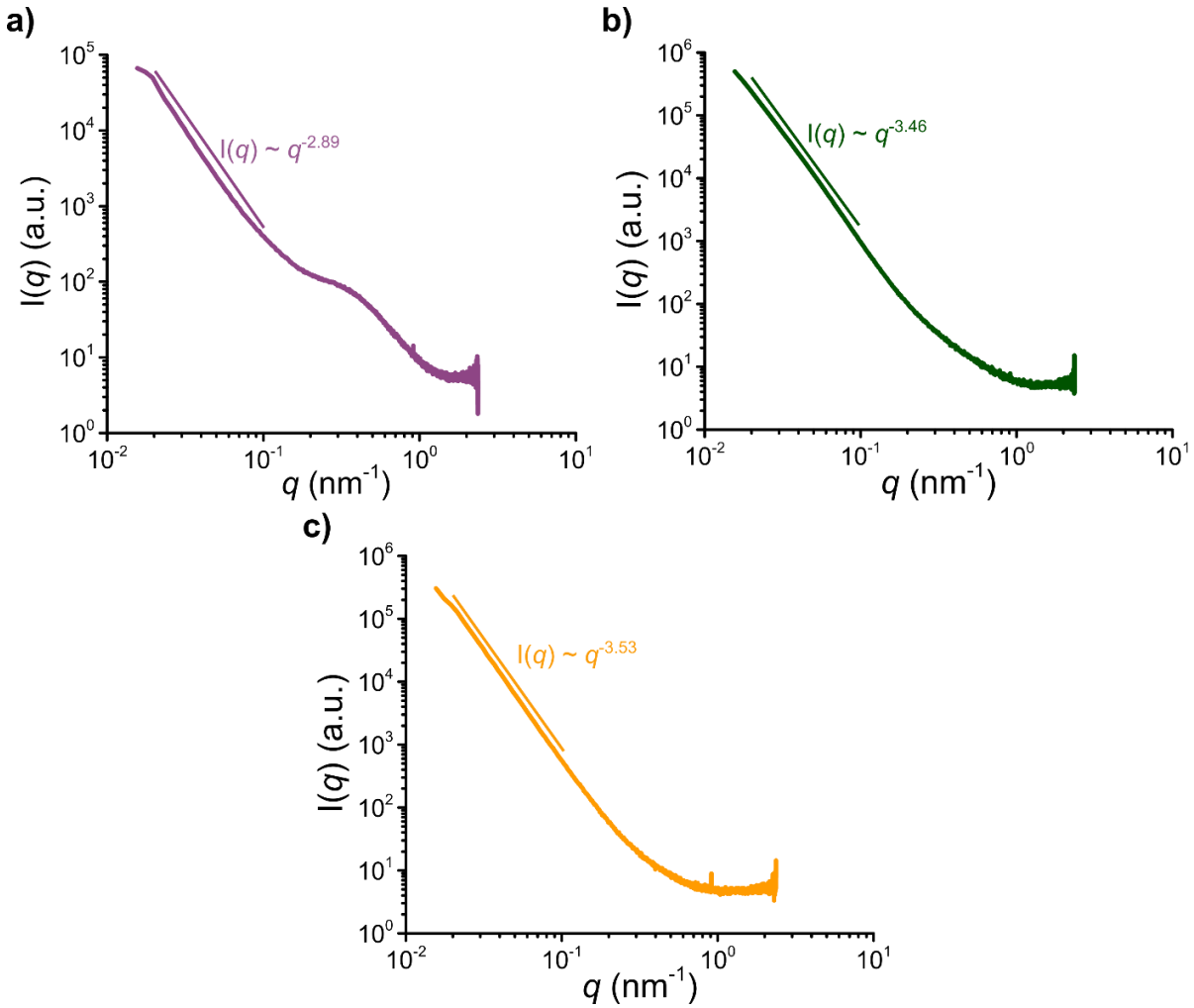

Figure S16. Small-Angle X-Ray Scattering curves, intensity of scattered rays as a function of scattering vector, of: **a) Vit$_{sol}$ b) Ext$_{<75\mu m}$; c) Ext$_{>75\mu m}$;**. The slopes of the initial part of the curve ($0.02 < q < 0.1$ nm^{-1}) were calculated by linear regression with $R^2 > 0.998$ for all curves.

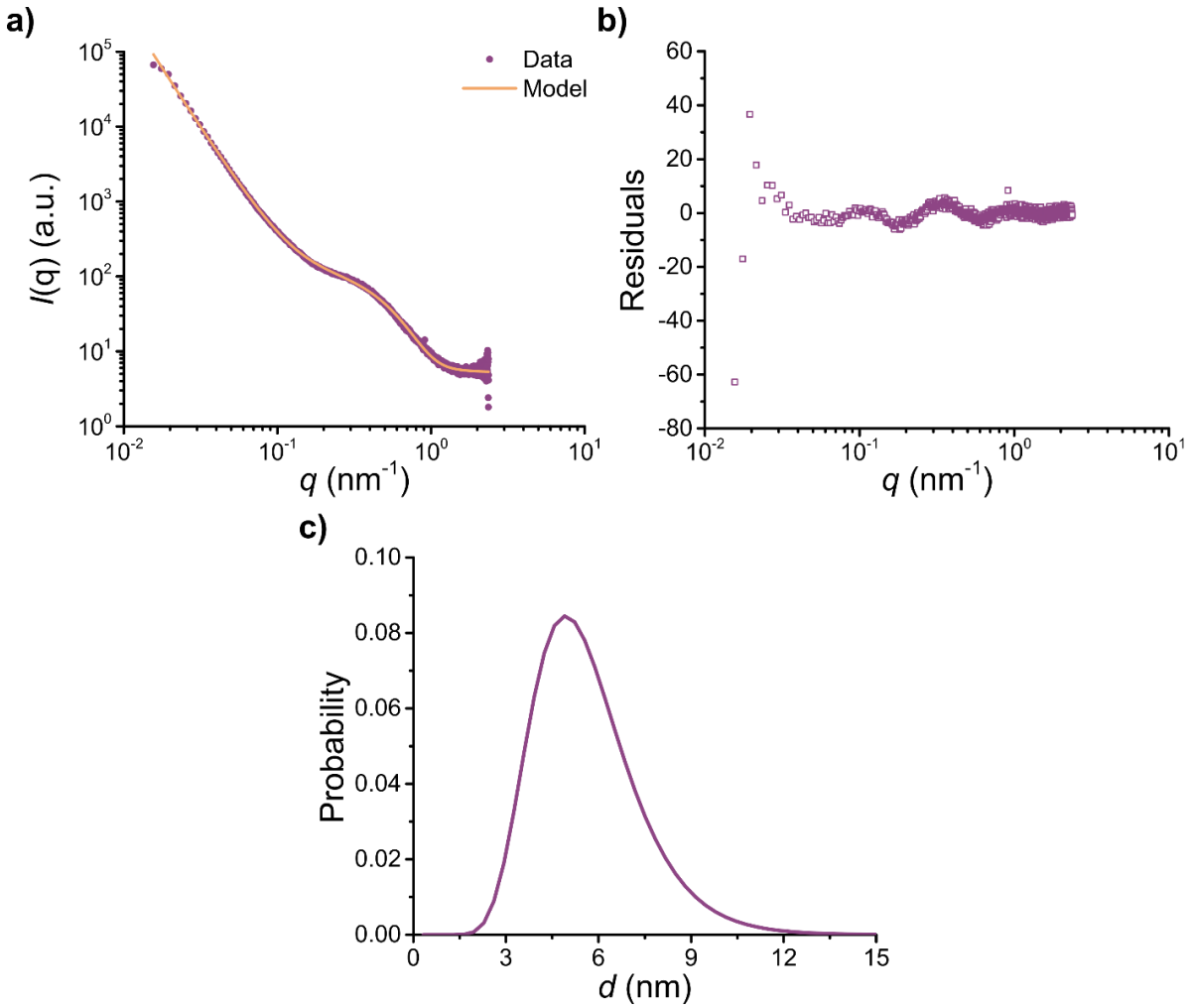

Figure S17. Model fitting of SAXS data of **Vit$_{sol}$**. **A.** Small-Angle X-Ray Scattering data as circles and fitted model as the orange line. The model that was used corresponds to the fractal aggregation of polydisperse spheres (following a log-normal distribution). **B.** Residuals of the fitted model. **C.** Log-normal distribution of the diameter of the spheres, obtained from the fitting.

Table S3. Fitting parameters of SAXS data of **Vit$_{sol}$**. Errors are the standard errors to the fit.

Parameter	D_{mean} (nm)	D_{median} (nm)	Dispersity[1]	Fractal dimension
Vit$_{sol}$	5.64±0.04	5.39±0.04	0.30±0.00[2]	2.96±0.00[2]

[1]Dispersity is calculated by dividing the standard deviation by the mean. [2]Errors are < 0.005.
The correlation length given by the model was orders of magnitude larger than the size limit of SAXS so it was not considered.

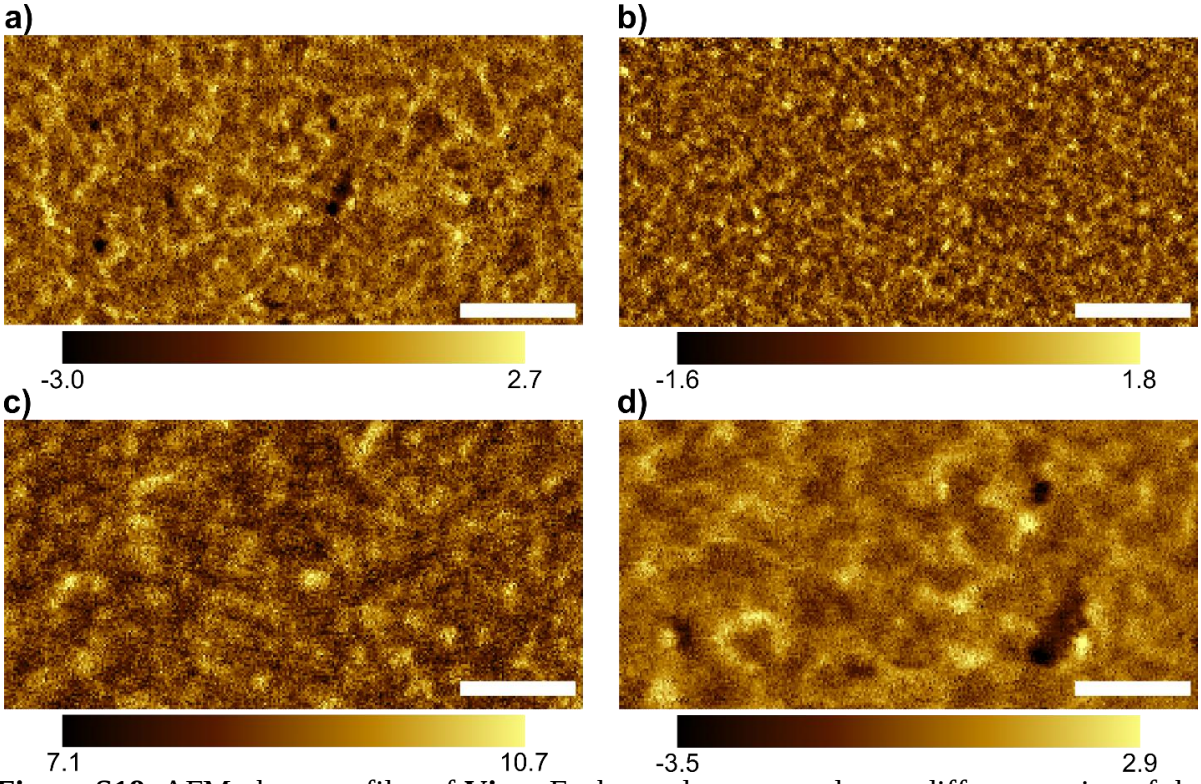

Figure S18. AFM phase profiles of **Vit$_{sol}$**. Each panel corresponds to a different region of the sample. The scale bars are 200 nm in a) and b) and 100 nm in c) and d). The color bar is the phase angle response.

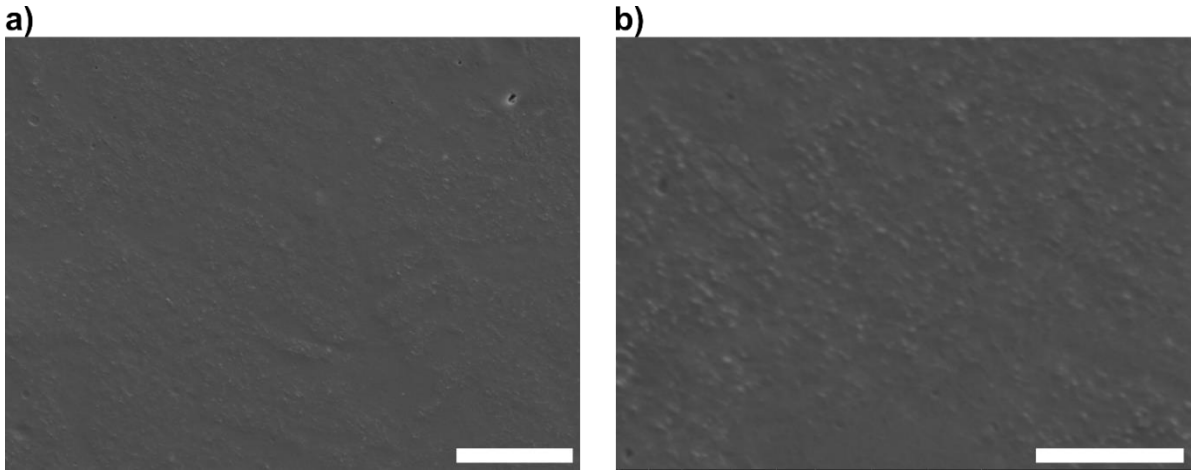

Figure S19. SEM of a cryogenically fractured **Vit$_{sol}$** surface. The scale bars are a) 5 µm and b) 2 µm.

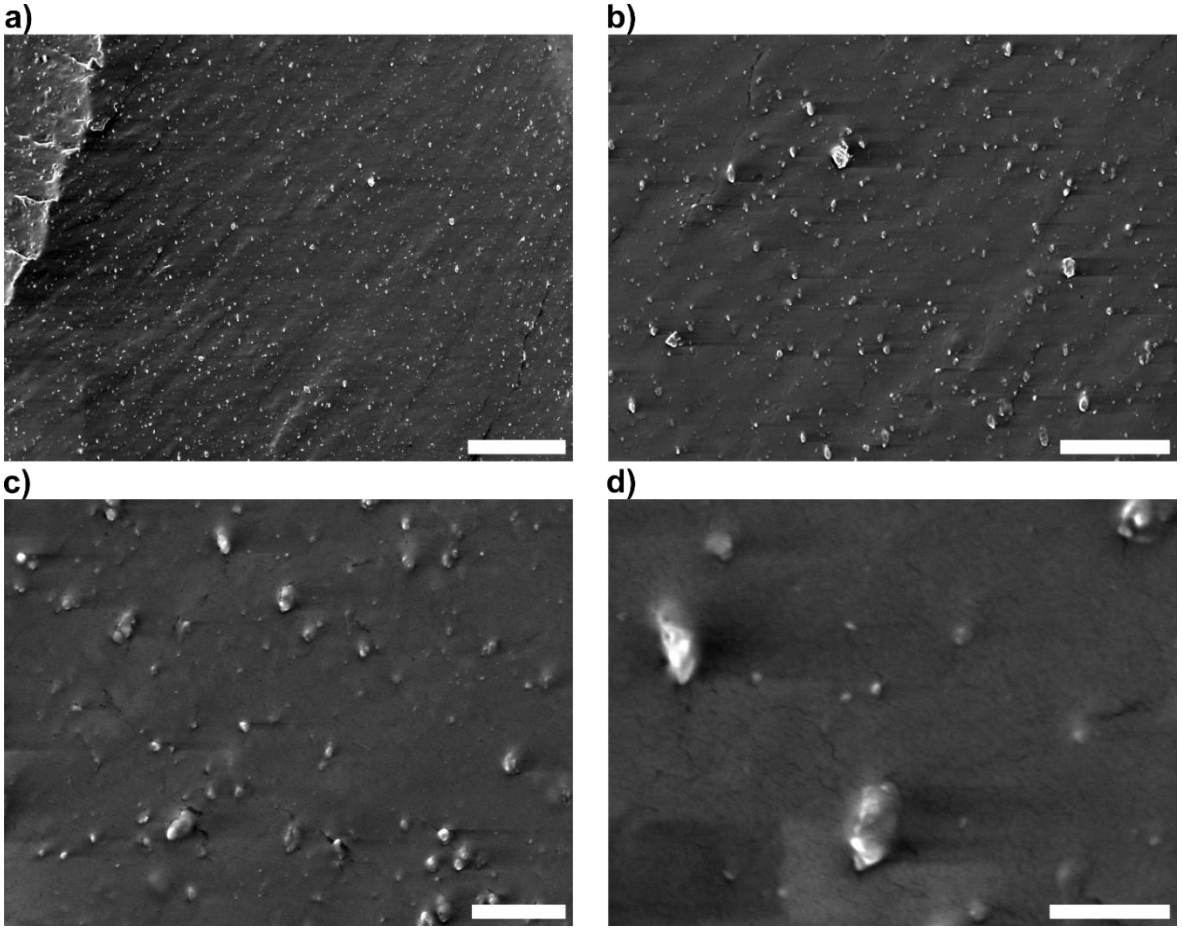

Figure S20. SEM of a soft fractured **Ext**$_{<75\mu m}$ surface. The scale bars are a) 50 µm, b) 20 µm, c) 5 µm, and d) 2 µm.

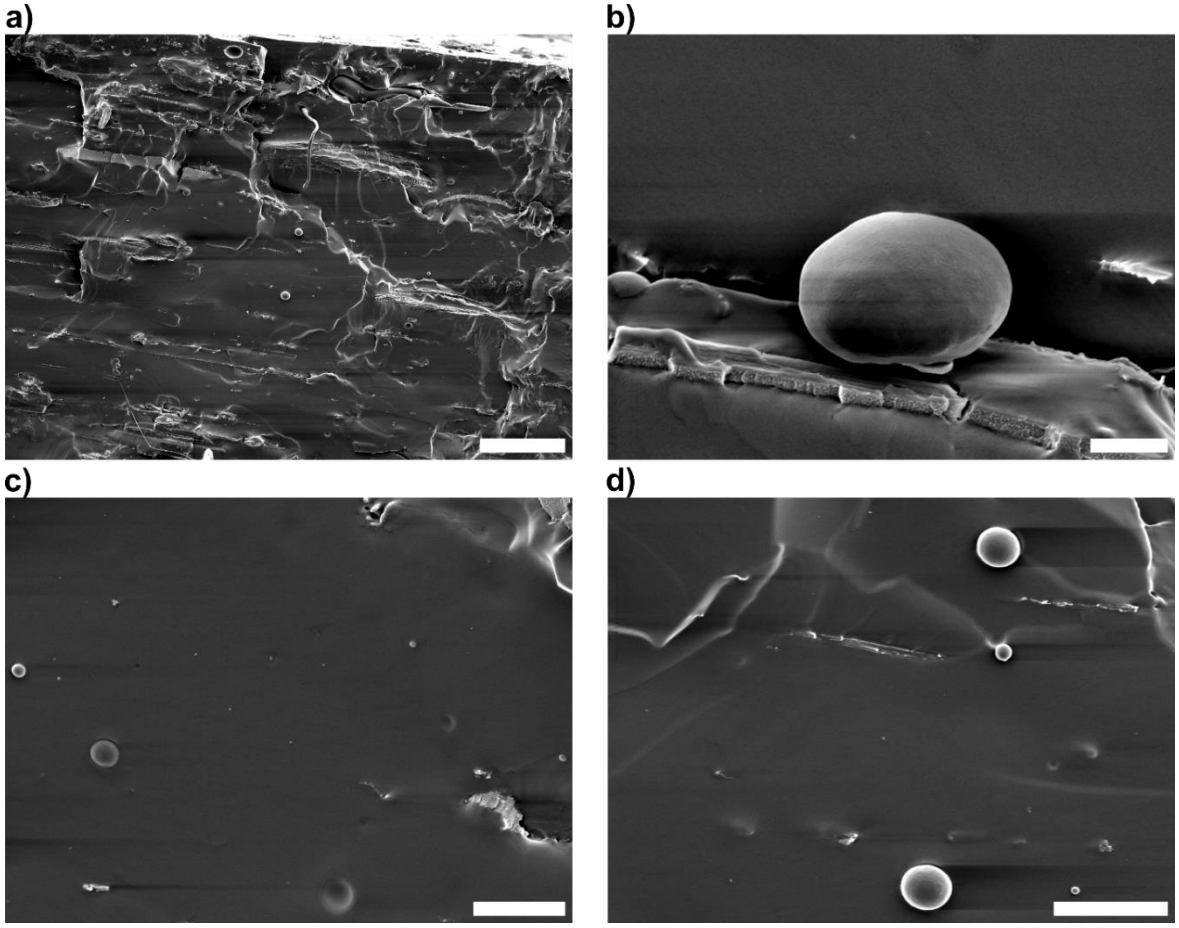

Figure S21. SEM of a soft fractured **Ext$_{>75\mu m}$** surface. The scale bars are a) 100 µm, b) 5 µm, c) 15 µm, and d) 25 µm.

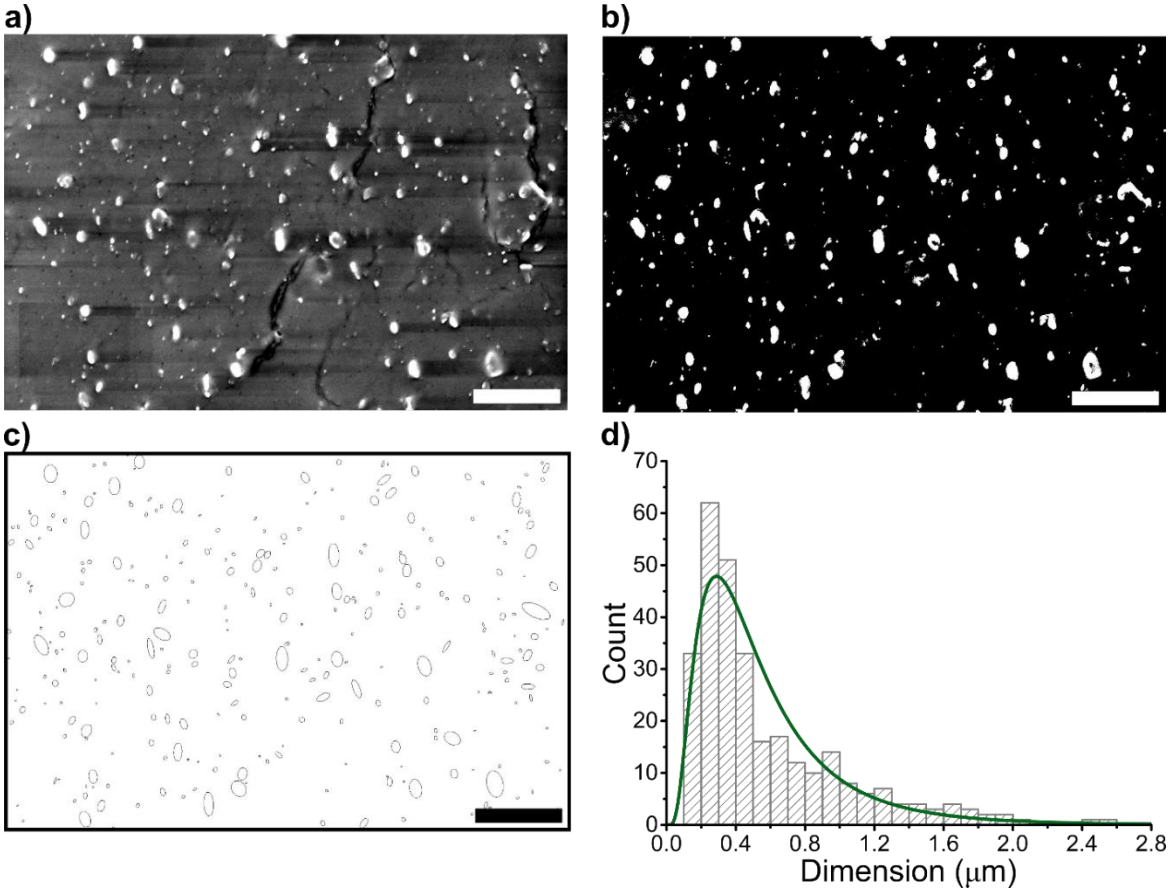

Figure S22. Representative image processing of the particle counting procedure for **Ext**$_{<75\mu m}$ performed using ImageJ.[S5,S10] a) Original SEM of a soft fractured **Ext**$_{<75\mu m}$ surface. b) Resulting image after automatic thresholding using Otsu's method.[S6,S11] c) Fitted ellipses obtained by the internal particle analyzer in ImageJ. d) Histogram of the characteristic dimension of the fitted ellipses (average of the minor and major axis of each ellipse), the bin size is 0.1 μm. The line is a log-normal distribution fitted to the data. The scale bars in a), b), and c) are 10 μm.

Table S4. Statistics of particle counting and ellipse fitting from SEM images for **Ext**$_{<75\mu m}$ and **Ext**$_{>75\mu m}$.[1]

Sample	Sample size	Mean characteristic dimension (μm)	Standard deviation (μm)	Median characteristic dimension (μm)	Minimum (μm)	Maximum (μm)
Ext$_{<75\mu m}$	1337	0.48	0.37	0.36	0.12	3.87
Ext$_{>75\mu m}$ [2]	38	3.97	3.78	2.71	0.36	16.94

[1]The characteristic dimension is the average of the major and minor axis of each individual fitted ellipse. [2]Counting and ellipse fitting was performed manually for **Ext**$_{>75\ \mu m}$ given the reduced number of particles due to the larger average size.

10. Thermomechanical characterization of vitrimers

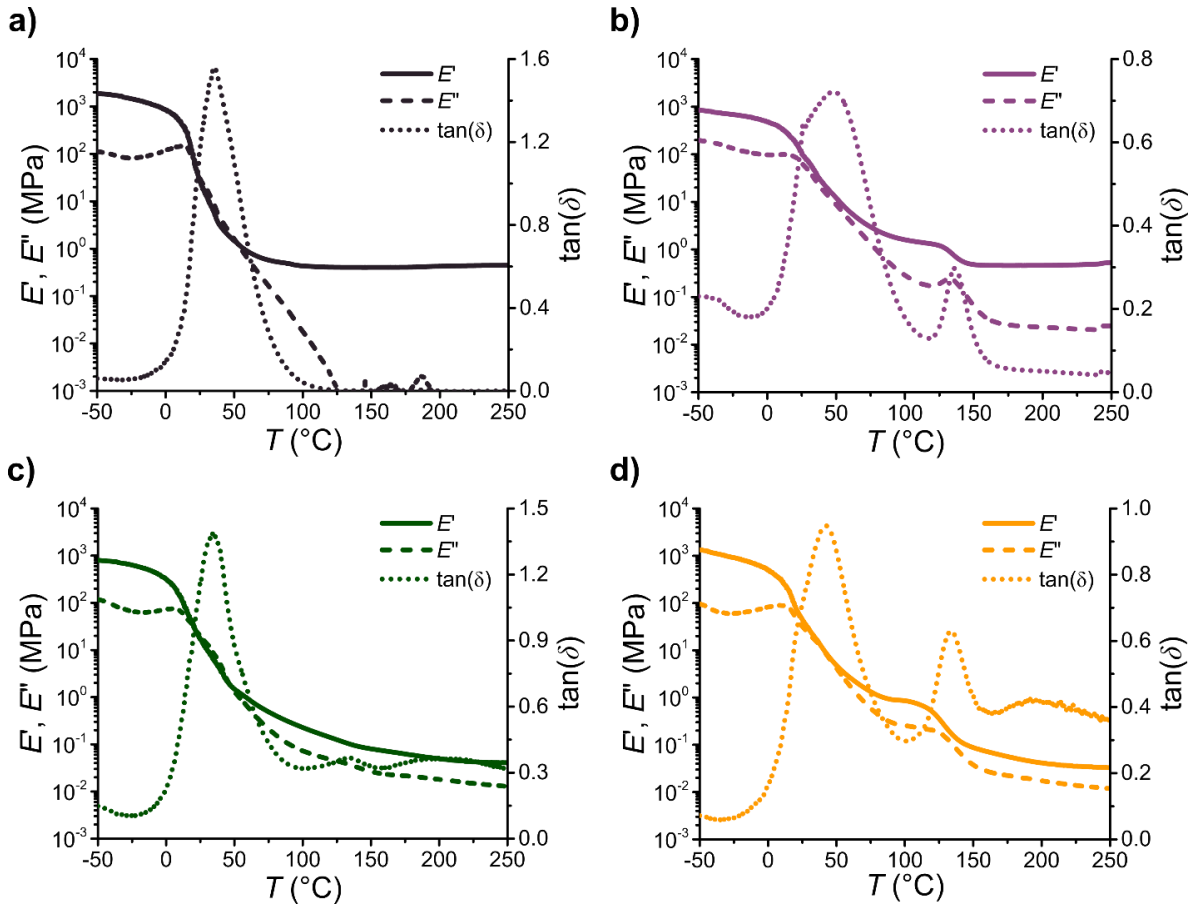

Figure S23. DMA traces of a) **BisBE Vit**; b) **Vit$_{sol}$**; c) **Ext$_{<75µm}$**; d) **Ext$_{>75µm}$**. The left axis shows elongation storage and loss moduli. Loss factor is represented on the right axis.

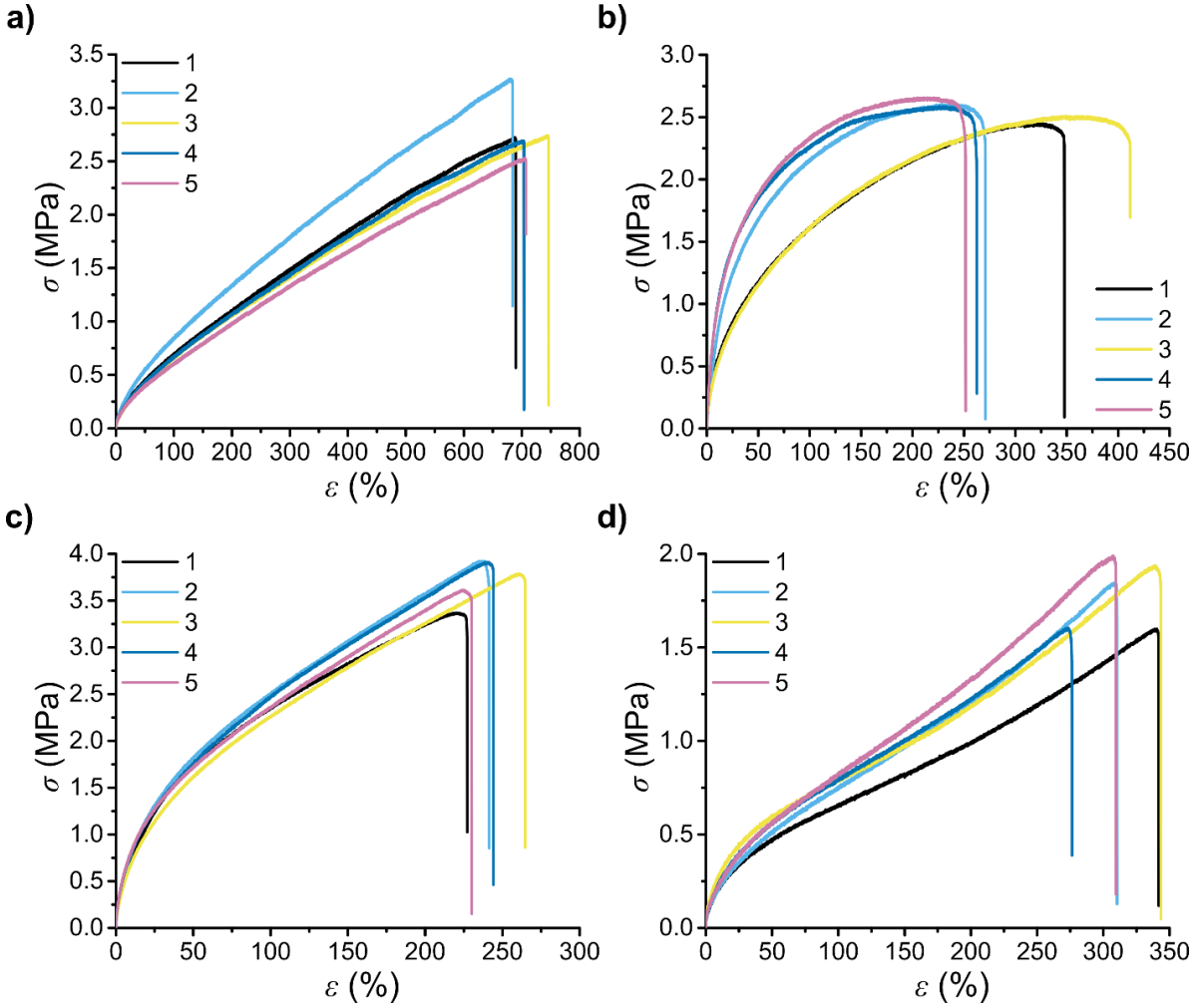

Figure S24. Engineering stress-strain curves of uniaxial tensile test of a) **Ext**$_{<75\mu m}$; b) **Ext**$_{>75\mu m}$; c) **Vit**$_{sol}$; d) **BisBE Vit**.

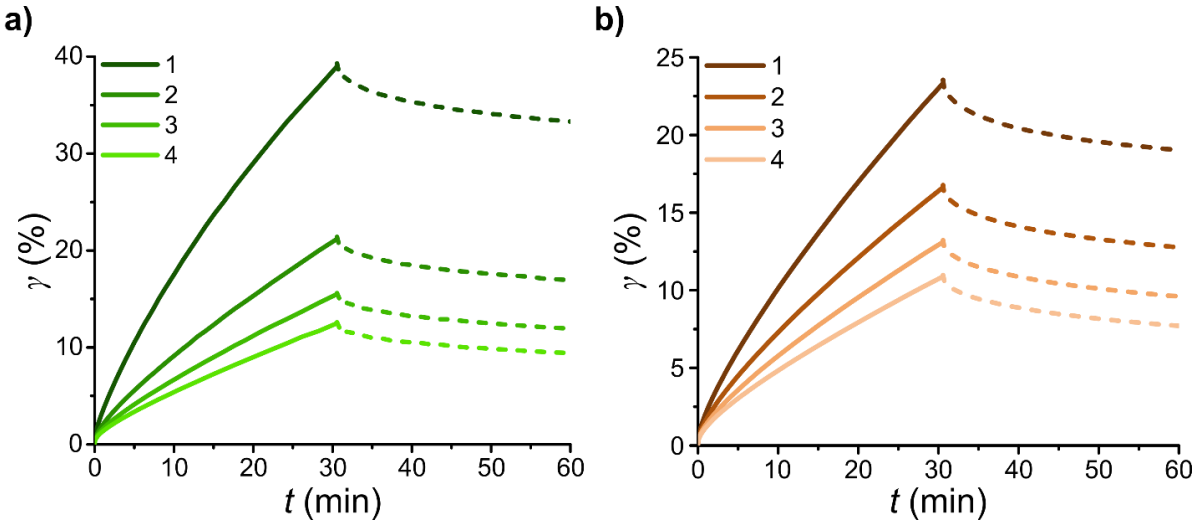

Figure S25. Creep and recovery cycles, strain as a function of time, at 160 °C with and applied stress of 50 Pa of a) **Ext**$_{<75\mu m}$ and b) **Ext**$_{>75\mu m}$. Creep is the full line and recovery is dashed.

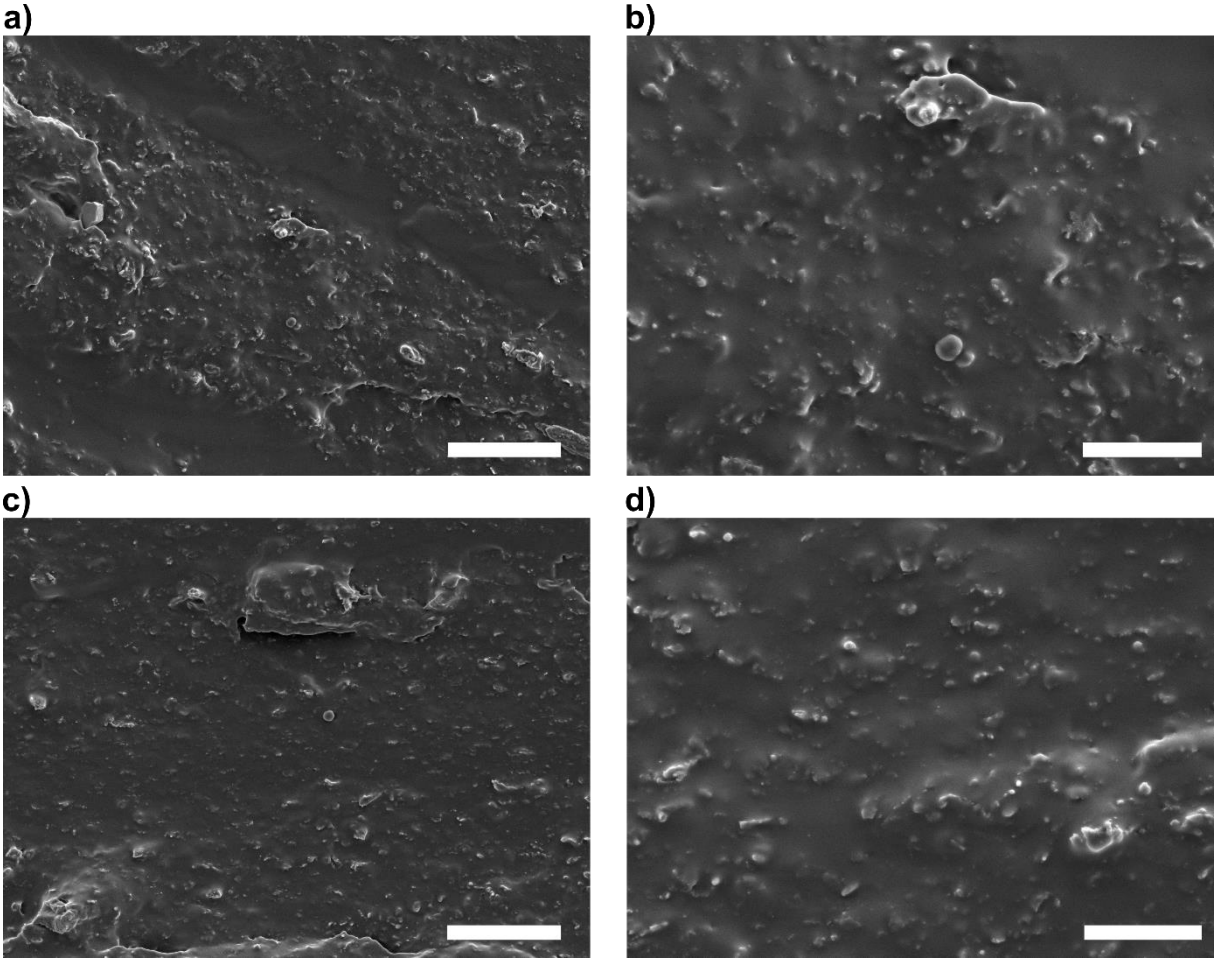

Figure S26. SEM of a soft fractured surface of a sample of **Ext**$_{<75\mu m}$ that was submitted to creep experiments shown in Figure S25. The scale bars are a) 25 µm, b) 10 µm, c) 25 µm, and d) 10 µm.

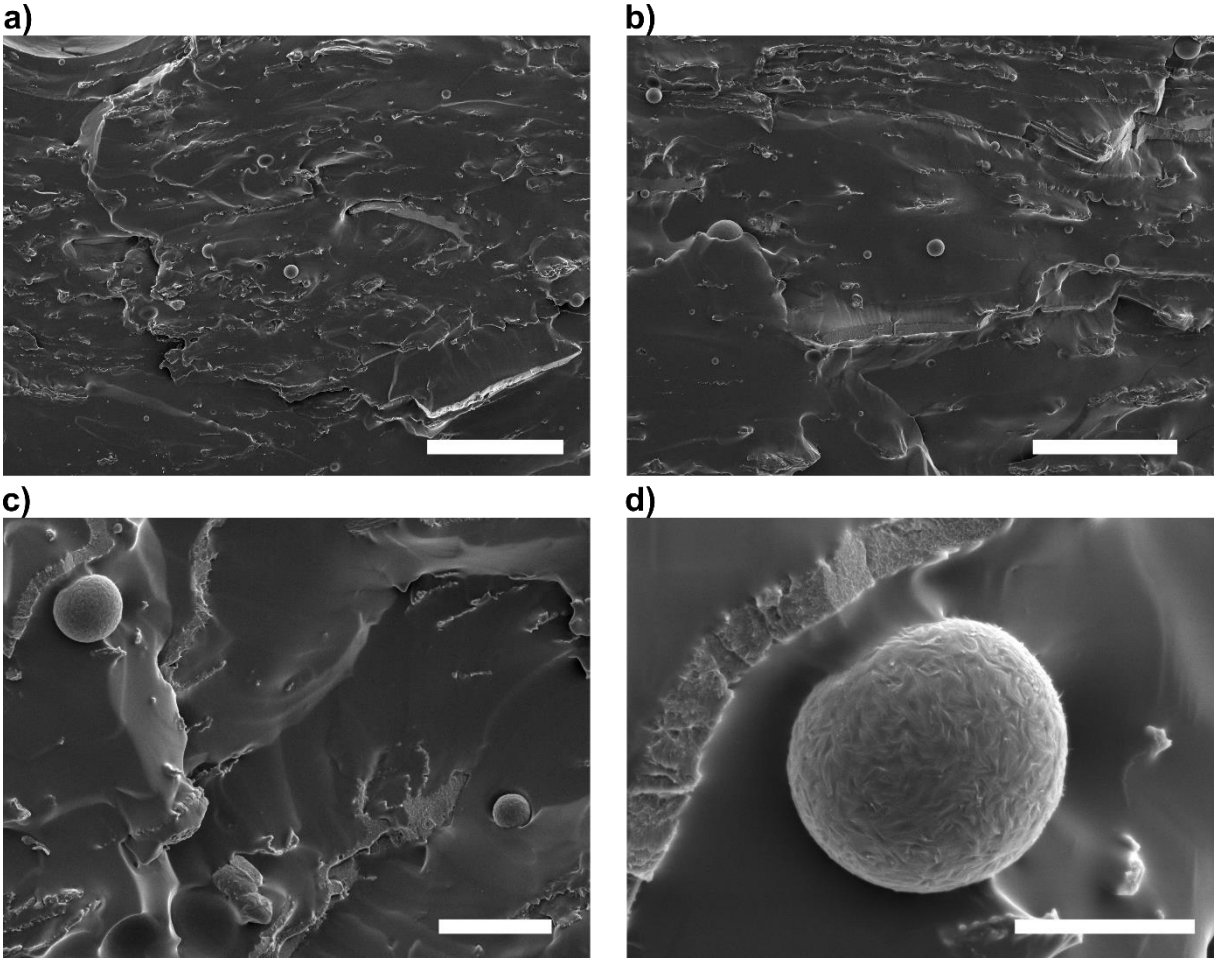

Figure S27. SEM of a soft fractured surface of a sample of **Ext**$_{>75\mu m}$ that was submitted to creep experiments shown in Figure S25. The scale bars are a) 150 µm, b) 100 µm, c) 25 µm, and d) 10 µm.

Table S5. Statistics of particle counting and ellipse fitting from SEM images for **Ext**$_{<75\mu m}$ and **Ext**$_{>75\mu m}$ on samples submitted to creep experiments.[1]

Sample	Sample size	Mean characteristic dimension (µm)	Standard deviation (µm)	Median characteristic dimension (µm)	Minimum (µm)	Maximum (µm)
Ext$_{<75\mu m}$ after Creep	5695	0.56	0.40	0.44	0.11	5.05
Ext$_{>75\mu m}$ after Creep [2]	65	6.78	5.14	4.88	1.35	24.49

[1]The characteristic dimension is the average of the major and minor axis of each individual fitted ellipse. [2]Counting and ellipse fitting was performed manually for **Ext**$_{>75\ \mu m}$ given the reduced number of particles due to the larger average size.

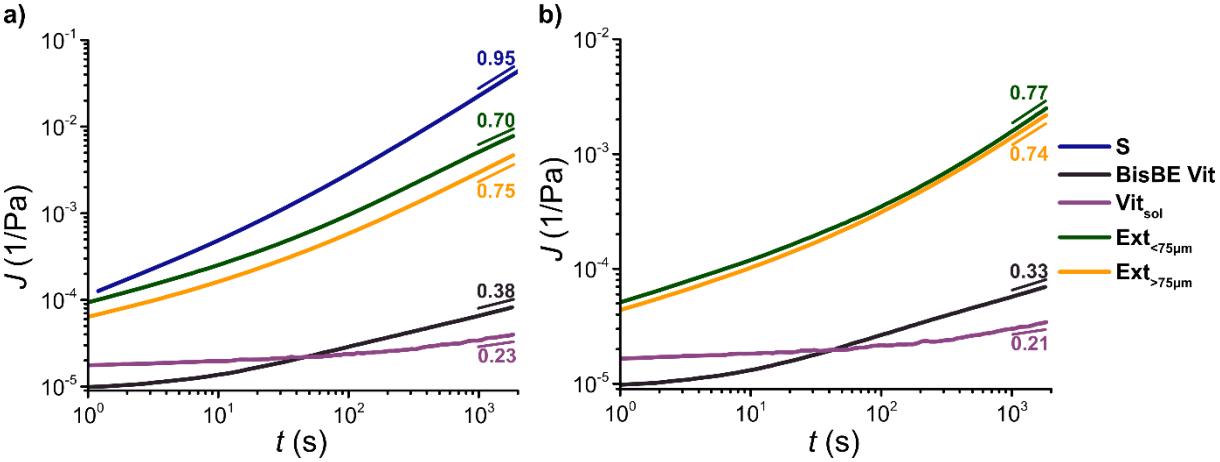

Figure S28. Log-log plot of the creep compliance (*J*) as a function of time of **S**, **BisBE Vit**, **Vit$_{sol}$**, **Ext$_{<75µm}$**, and **Ext$_{>75µm}$** of the a) first and b) fourth cycles. The number at the end part of each curve is the exponent of the fitted power law ($1000 \leq t \leq 1800$ s).[S12] $R^2 \geq 0.96$ for all samples.

11. References

[S1] T. H. N. Nguyen, R. Nicolaÿ, L. Deves, *FR3016885B1*, **2014**.

[S2] M. Röttger, T. Domenech, R. van der Weegen, A. Breuillac, R. Nicolaÿ, L. Leibler, *Science* **2017**, *356*, 62.

[S3] G. R. Fulmer, A. J. M. Miller, N. H. Sherden, H. E. Gottlieb, A. Nudelman, B. M. Stoltz, J. E. Bercaw, K. I. Goldberg, *Organometallics* **2010**, *29*, 2176.

[S4] F. Lednicky, G. H. Michler, *J. Mater. Sci.* **1990**, *25*, 4549.

[S5] J. Schindelin, I. Arganda-Carreras, E. Frise, V. Kaynig, M. Longair, T. Pietzsch, S. Preibisch, C. Rueden, S. Saalfeld, B. Schmid, J.-Y. Tinevez, D. J. White, V. Hartenstein, K. Eliceiri, P. Tomancak, A. Cardona, *Nat. Methods* **2012**, *9*, 676.

[S6] B. Sankur, *J. Electron. Imaging* **2004**, *13*, 146.

[S7] J. Brandrup, E. H. Immergut, E. A. Grulke, Eds., *Polymer Handbook, 4th Edition*, Wiley, New York ; Chichester, **2004**.

[S8] K. F. O'Driscoll, L. T. Kale, L. H. Garcia Rubio, P. M. Reilly. *J. Polym. Sci. Polym. Chem. Ed.* **1984**, *22*, 2777.

[S9] S. Beißmann, M. Stiftinger, K. Grabmayer, G. Wallner, D. Nitsche, W. Buchberger, *Polym. Degrad. Stab.* **2013**, *98*, 1655.

[S10] C. A. Schneider, W. S. Rasband, K. W. Eliceiri, *Nat. Methods* **2012**, *9*, 671.

[S11] N. Otsu, *IEEE Trans. Syst. Man Cybern.* **1979**, *9*, 62.

[S12] R. G. Ricarte, F. Tournilhac, M. Cloître, L. Leibler, *Macromolecules* **2020**, *53*, 1852.